Structural Robustness of Isotropic S^3 Vacua in Einstein–Cartan Minisuperspace via Chiral Equilibrium and Weyl Stability

Muacca

Abstract

We examine the robustness of the isotropic $S^3 \times S^1$ vacuum established in our preceding work (paper I) within the Einstein–Cartan + Nieh–Yan (EC+NY) Euclidean minisuperspace framework. Two independent extensions are analysed: a topological one (self-dual instanton decay paths) and a dynamical one (higher-curvature Weyl-squared corrections).

First, we prove that the Pontryagin density $P = \langle R, *R \rangle$ vanishes identically under the $M^3 \times S^1$ minisuperspace ansatz with EC connection—a property we term *chiral equilibrium*—thereby closing the self-dual instanton decay channel within this framework (Proposition 1).

Second, we introduce a Weyl-squared term $\alpha\, C^2$ and a volume-preserving squashed ansatz parameterised by an anisotropy variable ε. For $\alpha \leq 0$ the conformal flatness $C^2 = 0$ of isotropic $S^3 \times S^1$ renders the Weyl term inert, analytically protecting the global minimum of paper I (Theorem 1). For $\alpha > 0$ the effective potential becomes unbounded below (Theorem 2). The stability boundary $\alpha = 0$ is sharp and independent of the paper I matter parameters $(V, \eta, \theta_{\mathrm{NY}})$, a consequence of the geometric decoupling of the Weyl scalar from torsion (Theorem 3).

A systematic comparison of three topologies $(S^3, T^3, \mathrm{Nil}^3)$ confirms that the topology-selection principle—the energetic dominance of S^3—is preserved under the Weyl extension.

1 Introduction

1.1 Background: Results of Paper I and Two Open Questions

In paper I [1], we analysed the Einstein–Cartan (EC) gravity supplemented with the Nieh–Yan (NY) term [4] in a Euclidean-signature minisuperspace framework and established a systematic phase classification of the effective potential $V_{\text{eff}}(r)$. In particular, by comparing three spatial topologies—S^3 (SU(2)), T^3 (flat), and Nil^3 (Heisenberg group)—within a unified reduction procedure, we showed that the $S^3 \times S^1$ configuration forms the energetically most favourable stable vacuum over a wide region of parameter space: the *topology-selection principle.*

Two natural questions regarding the physical robustness of these results were left open:

1. **Topological stability.** Could self-dual instanton solutions exist on $S^3 \times S^1$, mediating vacuum decay via quantum tunnelling [3]?

2. **Dynamical stability.** Is the stability of the isotropic vacuum preserved under higher-curvature corrections to general relativity, notably the Weyl-squared term $\alpha\, C^2$?

1.2 Approach of the Present Work

In this paper we address both questions through independent analyses and provide a comprehensive demonstration of the robustness of the $S^3 \times S^1$ isotropic vacuum.

Topological stability. We show that the Pontryagin density $P = \langle R, *R \rangle$ vanishes identically under the $M^3 \times S^1$ minisuperspace ansatz with EC connection. This algebraic identity—reflecting what we call *chiral equilibrium* between self-dual and anti-self-dual curvature components—implies that self-dual instanton solutions are forbidden within this framework.

Dynamical stability. We extend the EC+NY Lagrangian by a Weyl-squared term $\alpha\, C^2$ and introduce a volume-preserving squashed ansatz with anisotropy parameter ε, constructing the two-variable effective potential $V_{\text{eff}}(r, \varepsilon; \alpha)$. The stability structure is classified by the sign of α:

- $\alpha \leq 0$: The conformal flatness $C^2 = 0$ of isotropic S^3 shields the vacuum from the Weyl term. For $\alpha < 0$ the Weyl penalty on $\varepsilon \neq 0$ directions further stabilises isotropy.

- $\alpha > 0$: The Weyl term asymptotically dominates V_{EC} as $r \to 0$, rendering the effective potential unbounded below ($V_{\text{eff}} \to -\infty$). This is the minisuperspace manifestation of the Ostrogradsky ghost instability of Weyl gravity.

1.3 Main Results: Four Theoretical Pillars

The principal results of this paper are summarised by the following four statements:

1. **Proposition 1 (Chiral equilibrium, $P = 0$).** Under the $M^3 \times S^1$ minisuperspace ansatz with EC connection, the Pontryagin density satisfies $P = \langle R, *R \rangle = 0$ identically. Self-dual instanton decay paths are closed within this ansatz.

2. **Theorem 1 (Weyl stability of the isotropic vacuum).** For $\alpha \leq 0$, the isotropic vacuum of $S^3 \times S^1$ is shielded from the Weyl term by conformal flatness, and the global minimum of V_{EC} is analytically protected.

3. **Theorem 2 (Unbounded instability for $\alpha > 0$).** For $\alpha > 0$, V_{eff} is unbounded below ($\inf V_{\text{eff}} = -\infty$); for $\alpha \leq 0$ and bounded V_{EC}, V_{eff} is bounded below. Hence $\alpha = 0$ is the sharp stability boundary.

4. **Theorem 3 (Parameter independence of the stability boundary).** The stability boundary $\alpha = 0$ is independent of the paper I parameters $(V, \eta, \theta_{\text{NY}})$, owing to the geometric decoupling of C^2 from torsion.

1.4 Logical Flow

1.5 Organisation of the Paper

The remainder of this paper is organised as follows.

- **§2 (Framework)**: EC+NY+Weyl Lagrangian and the squashed ansatz.

- **§3 (Chiral Equilibrium)**: Analytic proof of $P = 0$ (Proposition 1).

- **§4 (Weyl Extension)**: Closed-form Weyl scalar $C^2(r, \varepsilon)$ and effective potential structure.

- **§5 (Stability, $\alpha \leq 0$)**: Proof of Theorem 1.

- **§6 (Instability, $\alpha > 0$)**: Proof of Theorem 2.

- **§7 (Universality)**: Proof of Theorem 3.

- **§8 (Topology Comparison)**: Robustness of the topology-selection principle under Weyl extension.

- **§9 (Discussion)**: Repulsive core ($\alpha < 0$), Lorentzian extension, limitations.

- **§10 (Conclusion)**: Summary.

The DPPUv2 computation engine v4 specification is given in Appendix A, numerical verification details in Appendix B, and symbolic computation details in Appendix C.
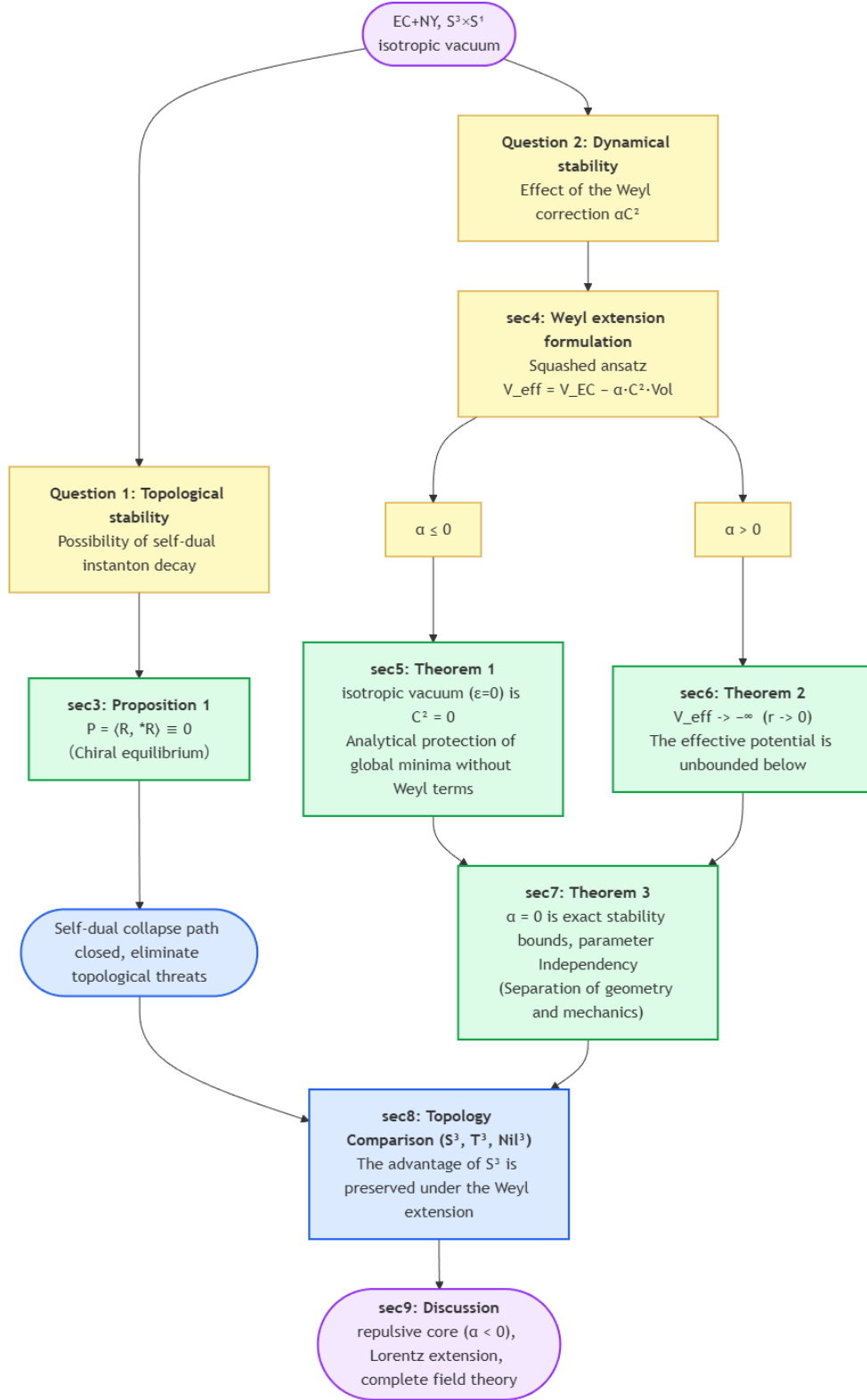
Figure 1: Logical flow of the paper. Starting from the EC+NY isotropic $S^3 \times S^1$ vacuum (paper I), the topological threat (Question 1) is addressed by Proposition 1 (§3), while the dynamical threat (Question 2) is resolved by Theorems 1–3 (§5–§7). The topology comparison (§8) confirms preservation of the S^3 dominance.

2 Framework

This section formulates the extended Lagrangian obtained by adding a Weyl-squared term to the EC+NY theory of paper I, and introduces the volume-preserving squashed ansatz.

2.1 EC+NY+Weyl Lagrangian

The extended Lagrangian studied in this paper is

$$\mathcal{L} = \frac{R_{\text{EC}}}{2\kappa^2} + \theta_{\text{NY}}\, N + \alpha\, C^2 \,, \tag{1}$$

where each term is defined as follows:

- $R_{\text{EC}}/(2\kappa^2)$: the Ricci scalar computed from the Einstein–Cartan connection (including torsion), with gravitational coupling constant κ.

- $\theta_{\text{NY}}\, N$: the Nieh–Yan term, where $N = \mathrm{d}(e^a \wedge T_a)$ is the Nieh–Yan density (a 4-form) and θ_{NY} its coupling constant, following the notation of paper I [1].

- $\alpha\, C^2$: the Weyl-squared term, where $C^2 = C_{abcd}\, C^{abcd}$ is the Kretschner-type Weyl scalar computed from the Levi-Civita connection, and α is a dimensionless coupling constant.

The Weyl tensor is defined with respect to the Levi-Civita connection. This choice avoids torsion contamination that would generically break conformal invariance if the EC connection were used instead. The quantities R_{EC} and N are computed from the EC connection.

Sign conventions. We adopt the same conventions as paper I:

- Frame metric: $\eta_{ab} = \mathrm{diag}(+1, +1, +1, +1)$ (Euclidean signature).

- Riemann tensor: $R^a{}_{bcd} = \partial_c \Gamma^a{}_{bd} - \partial_d \Gamma^a{}_{bc} + \Gamma^a{}_{ec}\Gamma^e{}_{bd} - \Gamma^a{}_{ed}\Gamma^e{}_{bc}$.

- Contortion: $K_{abc} = \frac{1}{2}(T_{abc} + T_{bca} - T_{cab})$ (Hehl et al. [2]).

- Levi-Civita symbol: $\varepsilon_{0123} = +1$.

2.2 Review of the $M^3 \times S^1$ Minisuperspace Ansatz

Following paper I, we decompose the four-dimensional Euclidean manifold as $\mathcal{M}_4 = \mathcal{M}_3 \times S^1$, where $\mathcal{M}_3$ is a compact quotient of a three-dimensional Lie group admitting a left-invariant coframe $\{\sigma^i\}$ ($i = 0, 1, 2$), and S^1 has circumference L.

In paper I the isotropic coframe $e^a = r\, \sigma^a$ ($a = 0, 1, 2$), $e^3 = L\, \mathrm{d}\tau$ was employed, with the scale variable r serving as the principal argument of the effective potential $V_{\text{eff}}(r)$.

2.3 Squashed Ansatz

To diagnose the effect of the Weyl term, a deformation parameter away from isotropy is required. We introduce an axisymmetric, volume-preserving squashing on S^3:

$$e^0 = r\,(1{+}\varepsilon)^{1/3}\,\sigma^0, \quad e^1 = r\,(1{+}\varepsilon)^{1/3}\,\sigma^1, \quad e^2 = r\,(1{+}\varepsilon)^{-2/3}\,\sigma^2, \quad e^3 = L\,d\tau, \qquad (2)$$

where

- $r > 0$ is the scale variable (identical to paper I),

- ε is the anisotropy parameter; $\varepsilon = 0$ is the isotropic point and $\varepsilon > -1$ is required for physical significance:

    - $\varepsilon > 0$: oblate deformation (e^0, e^1 directions expand, e^2 contracts),
    - $\varepsilon < 0$: prolate deformation (e^2 expands, e^0, e^1 contract),
    - $\varepsilon = -1$: singular point (complete collapse of one direction).

Volume preservation. The squashing factors satisfy $(1{+}\varepsilon)^{1/3}{\times}(1{+}\varepsilon)^{1/3}{\times}(1{+}\varepsilon)^{-2/3} = 1$, so that the four-volume is ε-independent:

$$\mathrm{Vol}(\mathcal{M}_4) = 2\pi^2 L\,r^3 \qquad (\text{independent of } \varepsilon). \qquad (3)$$

This ensures that ε modifies the *shape* without changing the *size* (r).

Squashed structure constants. The squashing modifies the S^3 structure constants to

$$C^i{}_{jk}(\varepsilon) = \frac{4}{r}\,\varepsilon_{ijk} \times f_i(\varepsilon), \qquad (4)$$

with

$$f_0(\varepsilon) = f_1(\varepsilon) = (1{+}\varepsilon)^{2/3}, \qquad f_2(\varepsilon) = (1{+}\varepsilon)^{-4/3}. \qquad (5)$$

At the isotropic point $\varepsilon = 0$, $f_0 = f_1 = f_2 = 1$ and one recovers the paper I structure constants.

2.4 Notation Summary

Table 1 collects the principal symbols used throughout the paper.

The paper I parameters $(V, \eta, \theta_{\mathrm{NY}})$ are scanned in §7; §4–6 use the reference values listed above.

Table 1: Principal symbols and their numerical scan ranges.

Symbol	Meaning	Scan range
r	Scale variable	$[0.01,\ 10]$
ε	Anisotropy parameter	$[-0.95,\ 5.0]$
α	Weyl coupling constant	$[-1,\ 1]$
V	Vector-torsion amplitude	Fixed ($V = 4$)
η	Axial-torsion amplitude	Fixed ($\eta = -2$, varied in §7)
θ_{NY}	Nieh–Yan coupling	Fixed ($\theta_{\mathrm{NY}} = 1$)
κ	Gravitational coupling	Fixed ($\kappa = 1$)
L	S^1 circumference	Fixed ($L = 1$)

2.5 Separation of the Effective Potential

Under the squashed ansatz, the effective potential separates *exactly linearly* in α:

$$V_{\mathrm{eff}}(r, \varepsilon; \alpha) = V_{\mathrm{EC}}(r, \varepsilon) - \alpha\, C^2(r, \varepsilon) \cdot \mathrm{Vol}(r). \tag{6}$$

Note the sign: since the Euclidean effective potential is defined as $V_{\mathrm{eff}} = -\mathcal{L} \times \mathrm{Vol}$ (see Appendix A, §A.2), the $+\alpha\, C^2$ term in the Lagrangian (1) enters as $-\alpha\, C^2 \cdot \mathrm{Vol}$ in the effective potential.

The two constituents are:

- $V_{\mathrm{EC}}(r, \varepsilon)$: the EC+NY effective potential, independent of α.

$$V_{\mathrm{EC}} = -\left(\frac{R_{\mathrm{EC}}}{2\kappa^2} + \theta_{\mathrm{NY}}\, N \right) \times \mathrm{Vol}. \tag{7}$$

- $C^2(r, \varepsilon) \cdot \mathrm{Vol}(r)$: a purely geometric quantity, independent of the paper I parameters $(V, \eta, \theta_{\mathrm{NY}})$.

This separation is the foundation of our analysis:

1. V_{EC} inherits the full content of paper I.

2. $C^2 \cdot \mathrm{Vol}$ is a geometric invariant decoupled from the torsion parameters.

3. The stability classification reduces to the sign of α.

The computational engine (DPPUv2 Engine v4)—including the derivation of the Levi-Civita connection, construction of the EC connection, and evaluation of the Weyl tensor—is documented in Appendix A.

3 Chiral Equilibrium: $P = 0$

In this section we prove that the Pontryagin density $P = \langle R, *R \rangle$ vanishes identically under the $M^3 \times S^1$ minisuperspace ansatz with EC connection. This eliminates the topological threat of vacuum decay through self-dual instanton tunnelling within the present framework.

3.1 Pontryagin Density and Self-Duality

On a four-dimensional Euclidean manifold, the Pontryagin density is defined as the inner product of the curvature 2-form R^{ab} with its Hodge dual $*R^{ab}$:

$$P = \langle R, *R \rangle = \tfrac{1}{4}\, \varepsilon^{abcd}\, R_{abef}\, R_{cd}{}^{ef}\,. \tag{8}$$

P is the density of the Pontryagin class and is related to self-duality as follows:

- $R = *R$ (self-dual) $\;\Leftrightarrow\; P = E > 0$,

- $R = -*R$ (anti-self-dual) $\;\Leftrightarrow\; P = -E < 0$,

where $E = \langle R, R \rangle = R_{abcd}\, R^{abcd}$ is the scalar related to the Euler (Gauss–Bonnet) density.

When (anti-)self-dual instanton solutions exist, they furnish finite-action extrema that can mediate vacuum decay via quantum tunnelling. Since $P \neq 0$ is a necessary condition for self-duality, the identity $P = 0$ excludes such solutions.

3.2 Proposition 1 (Chiral Equilibrium)

Proposition 1 (Chiral equilibrium). *Under the $M^3 \times S^1$ minisuperspace ansatz with Einstein–Cartan connection, the Pontryagin density vanishes identically:*

$$P = \langle R, *R \rangle = 0\,. \tag{9}$$

This holds as an algebraic identity for:

- *all choices of M^3 (S^3, T^3, Nil^3),*

- *all torsion modes (MX, AX, VT),*

- *all Nieh–Yan variants (FULL, TT, REE),*

- *all parameter values ($r, L, \eta, V, \kappa, \theta_{\mathrm{NY}}$).*

3.3 Proof

Step 1: Orthogonal decomposition of 2-forms. Let (x^0, x^1, x^2, τ) denote coordinates on $M^4 = M^3 \times S^1$. The space of 2-forms decomposes into two mutually orthogonal blocks:

$$\Lambda^2(M^4) = \underbrace{\Lambda^2(M^3)}_{\text{Spatial (S)}} \oplus \underbrace{\Lambda^1(M^3) \wedge d\tau}_{\text{Mixed (M)}} . \tag{10}$$

Explicitly, the spatial block (S) consists of 2-forms with index pairs $\{(01), (02), (12)\}$, and the mixed block (M) of $\{(03), (13), (23)\}$.

Step 2: The Hodge dual exchanges blocks. The four-dimensional Hodge dual (with $\varepsilon_{0123} = +1$) acts as

$$\begin{aligned}
*(01) &= +(23), & *(03) &= +(12), \\
*(02) &= -(13), & *(13) &= -(02), \\
*(12) &= +(03), & *(23) &= +(01).
\end{aligned} \tag{11}$$

That is, the Hodge dual maps $\Lambda^2(M^3)$ to $\Lambda^1(M^3) \wedge d\tau$ and vice versa.

Step 3: Curvature lies in the spatial block. Under the minisuperspace ansatz, the S^1 direction τ is a Killing direction and the connection is spatially homogeneous. As a consequence, the curvature 2-form $R^{ab}{}_{cd}$ has non-vanishing lower-index pairs (c, d) only in the spatial block: $(c, d) \in \{(01), (02), (12)\}$. Components with (c, d) in the mixed block vanish identically.

This property has been verified by symbolic computation for all three topologies (see §3.5 and Appendix C).

Step 4: Orthogonality implies $P = 0$. Since R has lower indices in the spatial block only, $*R$ has lower indices in the mixed block only (Step 2). The two blocks are orthogonal, hence

$$\langle R, *R \rangle = 0 . \qquad \square \tag{12}$$

3.4 One-Line Summary

The proof may be condensed to a single chain of implications:

$$R \in \Lambda^2(M^3) \;\Rightarrow\; *R \in \Lambda^1(M^3) \wedge d\tau \;\Rightarrow\; \langle R, *R \rangle = 0 . \tag{13}$$

3.5 Symbolic Verification

Algebraic verification using symbolic computation software confirms $P = 0$ for all three topologies (full details in Appendix C):

Table 2: Symbolic verification of $P = 0$ across topologies.

Topology	Spatial components	Mixed components	$P = \langle R, *R \rangle$	Status
$S^3 \times S^1$	6	0	**0**	✓
$T^3 \times S^1$	6	0	**0**	✓
$\text{Nil}^3 \times S^1$	6	0	**0**	✓

Representative non-vanishing curvature components for $S^3 \times S^1$:

$$R^{01}{}_{01} = \frac{-V^2 r^2/9 - \eta^2 - 8\eta - 12}{r^2}, \qquad R^{03}{}_{12} = \frac{-2V(\eta + 4)}{3r}. \tag{14}$$

All non-vanishing lower-index pairs (c, d) belong to the spatial block $\{01, 02, 12\}$, with no mixed-block components.

3.6   Physical Interpretation

3.6.1   Chiral equilibrium

The identity $P = 0$ means that the self-dual and anti-self-dual components of the curvature are balanced in norm. Decomposing

$$R = R^+ + R^-, \qquad R^\pm = \tfrac{1}{2}(R \pm *R), \tag{15}$$

one finds $P = \langle R, *R \rangle = \|R^+\|^2 - \|R^-\|^2$, so that $P = 0$ implies

$$\|R^+\| = \|R^-\|. \tag{16}$$

Both chiralities are present in precisely equal measure; we call this *chiral equilibrium.*

3.6.2   Structural prohibition of self-dual instantons

Self-duality $R = *R$ requires $R^- = 0$, i.e. $\|R^-\| = 0$. By chiral equilibrium, $\|R^-\| = 0$ forces $\|R^+\| = 0$ simultaneously, hence $R = 0$. Therefore, *as long as the curvature is non-vanishing*, neither self-dual nor anti-self-dual solutions can exist on $M^3 \times S^1$ within the minisuperspace ansatz.

The $S^3 \times S^1$ isotropic vacuum is thus protected from instanton-mediated tunnelling decay. This protection is a *geometric consequence* of the product structure $M^3 \times S^1$ and the minisuperspace ansatz, independent of specific parameter values or torsion configurations.

3.7 Conditions for Breakdown of $P = 0$

Achieving $P \neq 0$ and thereby admitting self-dual solutions requires extending beyond the present geometric setting:

Table 3: Extensions that can break $P = 0$.

Direction of extension	Modification	Why $P = 0$ breaks
Inhomogeneous torsion	Position-dependent $T^a(x)$	Breaks homogeneity; mixed-block curvature appears
Non-product manifold	Beyond $M^3 \times S^1$	Product structure underlies the block restriction
Lorentzian signature	$(-, +, +, +)$	Eigenspace structure of Hodge $*$ changes
Non-compact M^3	Inhomogeneous geometry	Curvature structure may differ

These extensions are discussed as future directions in §9.

4 Weyl Extension: Squashed Ansatz

In this section we derive the closed-form expression for the Weyl scalar $C^2(r, \varepsilon)$ under the squashed ansatz of §2.3 and elucidate the structure of the effective potential.

4.1 Computation of the Weyl Tensor

The Weyl tensor is computed from the Levi-Civita connection via the following standard procedure:

1. **Levi-Civita connection** in the orthonormal frame (generalised Koszul formula):

$$\Gamma^a{}_{bc} = \tfrac{1}{2}\left(C^a{}_{bc} + C^c{}_{ba} - C^b{}_{ac}\right).\tag{17}$$

2. **Riemann tensor** in the frame basis:

$$R^a{}_{bcd} = \Gamma^a{}_{ec}\,\Gamma^e{}_{bd} - \Gamma^a{}_{ed}\,\Gamma^e{}_{bc} + \Gamma^a{}_{be}\,C^e{}_{cd}.\tag{18}$$

3. **Ricci tensor and scalar**: $R_{bd} = R^a{}_{bad}, \;\; R = R^a{}_a$.

4. **Weyl tensor** (4-dimensional definition):

$$C_{abcd} = R_{abcd} - \tfrac{1}{2}\left(g_{ac}R_{bd} - g_{ad}R_{bc} - g_{bc}R_{ad} + g_{bd}R_{ac}\right) + \tfrac{R}{6}\left(g_{ac}g_{bd} - g_{ad}g_{bc}\right).\tag{19}$$

5. **Weyl scalar**: $C^2 = C_{abcd}\,C^{abcd}$ (with $g^{ab} = \delta^{ab}$ in the orthonormal frame).

4.2 Lemma 1: Closed-Form Weyl Scalar

Lemma 1. *The four-dimensional Weyl scalar of the squashed $S^3 \times S^1$ metric, computed from the Levi-Civita connection, is*

$$C^2(r, \varepsilon) = \frac{1024\,\varepsilon^2(\varepsilon+2)^2}{3\,r^4\,(1+\varepsilon)^{16/3}}.\tag{20}$$

Proof. By symbolic algebraic computation following the procedure of §4.1, with the squashed structure constants (4) as input. All components of the Weyl tensor are computed, and the sum of squares is simplified and factored to yield (20). Full details are given in Appendix C. $\square$

4.3 Key Properties of Lemma 1

(i) Vanishing at the isotropic point: $C^2(r,0) = 0$. The factor ε^2 in the numerator ensures $C^2 = 0$ at $\varepsilon = 0$. Physically, the round S^3 is a space of constant curvature and

hence conformally flat; the product metric $S^3 \times S^1$ is therefore conformally flat in four dimensions, with identically vanishing Weyl tensor.

(ii) Non-negativity: $C^2(r, \varepsilon) \geq 0$ $(\varepsilon > -1)$. As a sum of squares in the orthonormal frame, $C^2 \geq 0$ by definition. The only zero (for $\varepsilon > -1$) is $\varepsilon = 0$; the other root $\varepsilon = -2$ lies beyond the singularity at $\varepsilon = -1$.

(iii) Quadratic behaviour at the isotropic point.

$$\left.\frac{\partial C^2}{\partial \varepsilon}\right|_{\varepsilon=0} = 0, \qquad \left.\frac{\partial^2 C^2}{\partial \varepsilon^2}\right|_{\varepsilon=0} = \frac{8192}{3r^4} > 0. \tag{21}$$

Hence C^2 has a quadratic minimum at the isotropic point:

$$C^2(r, \varepsilon) \approx \frac{8192}{3r^4}\, \varepsilon^2 \qquad (|\varepsilon| \ll 1). \tag{22}$$

(iv) Divergence as $r \to 0$. For fixed $\varepsilon \neq 0$, $C^2 \sim 1/r^4$. The product with the volume (3) gives

$$C^2 \cdot \text{Vol} = \frac{2048\pi^2 L\, \varepsilon^2 (\varepsilon+2)^2}{3\, r\, (1+\varepsilon)^{16/3}} \sim \frac{1}{r} \qquad (r \to 0). \tag{23}$$

This unboundedness is the key to the instability proof in §6.

4.4 Structure of Non-Vanishing Weyl Components

For general ε, there are 24 non-vanishing Weyl-tensor components, all sharing the common factor

$$C_{abcd} \propto \frac{\varepsilon(\varepsilon+2)}{r^2\, (1+\varepsilon)^{8/3}}. \tag{24}$$

Representative independent components:

Table 4: Representative non-vanishing Weyl-tensor components.

Component	Value
C_{0101}	$+\dfrac{16\,\varepsilon(\varepsilon+2)}{3r^2(1+\varepsilon)^{8/3}}$
C_{0202}, C_{0303}	$-\dfrac{8\,\varepsilon(\varepsilon+2)}{3r^2(1+\varepsilon)^{8/3}}$
C_{2323}	$+\dfrac{16\,\varepsilon(\varepsilon+2)}{3r^2(1+\varepsilon)^{8/3}}$
C_{1212}, C_{1313}	$-\dfrac{8\,\varepsilon(\varepsilon+2)}{3r^2(1+\varepsilon)^{8/3}}$

All components contain $\varepsilon(\varepsilon+2)$ as a factor and vanish at $\varepsilon = 0$. A complete listing is provided in Appendix C.

4.5 Effective Potential with Explicit Weyl Contribution

Substituting the result of Lemma 1 into the separation (6) yields

$$V_{\text{eff}}(r, \varepsilon; \alpha) = V_{\text{EC}}(r, \varepsilon) - \alpha \cdot \frac{2048\pi^2 L \, \varepsilon^2 (\varepsilon+2)^2}{3 \, r \, (1+\varepsilon)^{16/3}} \,. \tag{25}$$

The effect of the Weyl term depends on the sign of α:

Table 5: Effect of the Weyl term $-\alpha \, C^2 \cdot \text{Vol}$ on $\varepsilon \neq 0$ configurations.

Sign of α	Weyl contribution $-\alpha \, C^2 \cdot \text{Vol}$	Effect on $\varepsilon \neq 0$
$\alpha = 0$	0	None (paper I recovered)
$\alpha < 0$	$+|\alpha| \, C^2 \cdot \text{Vol} > 0$	Positive penalty (stabilises isotropy)
$\alpha > 0$	$-\alpha \, C^2 \cdot \text{Vol} < 0$	Negative reward (promotes anisotropy)

4.6 Effective Potential Contour Maps
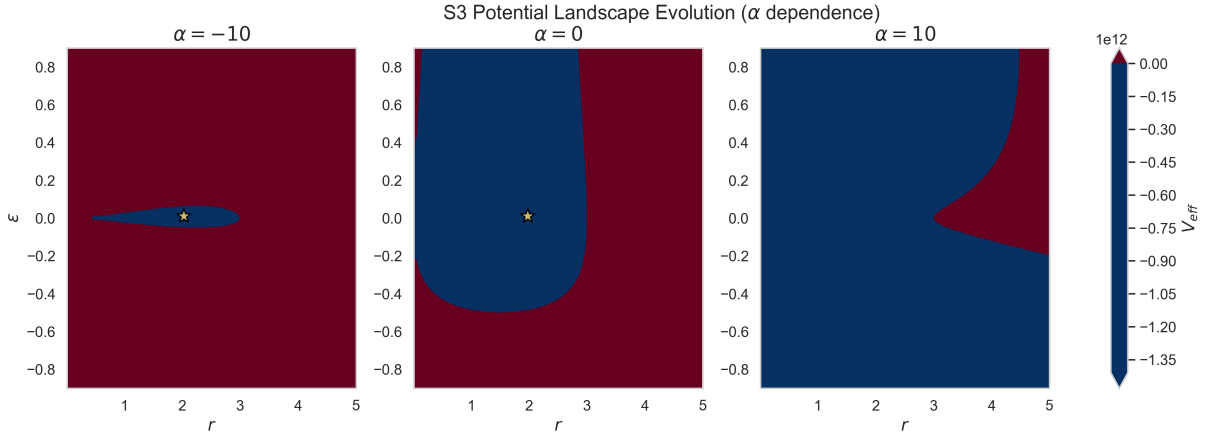
Figure 2: Contour maps of V_{eff} in the (r, ε) plane for S^3 at $\alpha = -10, 0,$ and $+10$. For $\alpha \leq 0$ the isotropic vacuum ($\varepsilon = 0$) forms a stable valley, while for $\alpha > 0$ the valley is destroyed and the potential landscape collapses. The analytic foundations of this qualitative change are established in §5 and §6.

5 Stability of the Isotropic Vacuum ($\alpha \leq 0$)

We now prove that for $\alpha \leq 0$ the isotropic vacuum of $S^3 \times S^1$ is analytically protected from the Weyl extension.

5.1 Theorem 1 (Weyl Stability of the Isotropic Vacuum)

Theorem 1 (Weyl stability)**.** *Under the EC+NY+Weyl Lagrangian* (1) *on $S^3 \times S^1$, the isotropic vacuum ($\varepsilon = 0$) satisfies:*

(a) The Weyl scalar vanishes identically at the isotropic point:

$$C^2(r, \varepsilon{=}0) = 0 \qquad (\forall\, r > 0)\,. \tag{26}$$

(b) For $\alpha \leq 0$, the Weyl term reinforces (or leaves unaffected) the isotropic minimum of the effective potential:

$$V_{\text{eff}}(r, \varepsilon; \alpha) = V_{\text{EC}}(r, \varepsilon) + |\alpha|\, C^2(r, \varepsilon) \cdot \text{Vol}(r)\,, \tag{27}$$

where $|\alpha|\, C^2 \cdot \text{Vol} \geq 0$, with equality if and only if $\varepsilon = 0$.

(c) As a corollary, if V_{EC} attains a global minimum at $(r_0, 0)$, then V_{eff} also attains its global minimum at $(r_0, 0)$ with the same minimum value $V_{\text{EC}}(r_0, 0)$, for all $\alpha \leq 0$.

5.2 Proof

Part (a). Setting $\varepsilon = 0$ in Lemma 1, the factor ε^2 in the numerator of (20) gives $C^2(r, 0) = 0$. $\qquad\qquad\qquad\qquad\qquad\qquad\qquad\qquad\qquad\qquad\qquad\qquad\qquad\qquad\square$

Part (b). For $\alpha \leq 0$, write $-\alpha = |\alpha| \geq 0$. Then

$$V_{\text{eff}}(r, \varepsilon; \alpha) = V_{\text{EC}}(r, \varepsilon) + |\alpha|\, C^2(r, \varepsilon) \cdot \text{Vol}(r)\,. \tag{28}$$

By Lemma 1 (ii), $C^2 \geq 0$. Since $\text{Vol}(r) = 2\pi^2 L r^3 > 0$, it follows that $|\alpha|\, C^2 \cdot \text{Vol} \geq 0$, with equality if and only if $C^2 = 0$, i.e. $\varepsilon = 0$. Hence:

- $V_{\text{eff}}(r, \varepsilon; \alpha) \geq V_{\text{EC}}(r, \varepsilon)$ for all r, ε;

- $V_{\text{eff}}(r, 0; \alpha) = V_{\text{EC}}(r, 0)$ for all r.

The Weyl term adds a positive penalty only in the $\varepsilon \neq 0$ directions and leaves the isotropic slice unchanged. $\qquad\qquad\qquad\qquad\qquad\qquad\qquad\qquad\qquad\qquad\qquad\qquad\qquad\qquad\square$

Part (c). Suppose V_{EC} has a global minimum at $(r_0, 0)$:

$$V_{\text{EC}}(r_0, 0) \leq V_{\text{EC}}(r, \varepsilon) \qquad \forall\, r, \varepsilon\,. \tag{29}$$

For any (r, ε):

$$V_{\text{eff}}(r, \varepsilon; \alpha) = V_{\text{EC}}(r, \varepsilon) + |\alpha|\, C^2 \cdot \text{Vol} \geq V_{\text{EC}}(r, \varepsilon) \geq V_{\text{EC}}(r_0, 0)\,. \tag{30}$$

On the other hand:

$$V_{\text{eff}}(r_0, 0; \alpha) = V_{\text{EC}}(r_0, 0) + |\alpha| \cdot 0 \cdot \text{Vol} = V_{\text{EC}}(r_0, 0)\,. \tag{31}$$

Hence $(r_0, 0)$ is a global minimum of V_{eff} with value $V_{\text{EC}}(r_0, 0)$.

Moreover, if the minimum of V_{EC} is strict (attained only at $(r_0, 0)$), the Weyl penalty $|\alpha|\, C^2 \cdot \text{Vol} > 0$ for $\varepsilon \neq 0$ makes the minimum of V_{eff} *even more* strictly isolated. $\qquad\square$

5.3 Assumptions of Theorem 1

The conclusion of part (c) relies on the premise that V_{EC} has a global minimum at $\varepsilon = 0$. This premise is:

- **Numerically verified**: the Stage 2D optimisation with reference parameters ($V{=}4$, $\eta{=}{-}2$, $\theta_{\text{NY}}{=}1$, $\kappa{=}1$, $L{=}1$) yields a minimum at $(r_0, \varepsilon) = (2.000, 0)$ with $V_{\min} = -421.103$.

- **Partially supported analytically**: the positive definiteness of the ε-direction Hessian of V_{EC} at the isotropic point provides a local-minimum proof. A complete analytic proof of global minimality remains an open problem.

5.4 Numerical Verification

The predictions of Theorem 1 are compared with Stage 2D numerical results:

Table 6: Theorem 1 predictions versus numerical results.

Prediction (from Theorem 1)	Numerical result	Agreement
$V_{\min}$ constant for $\alpha \leq 0$	-421.103 at all 201 points ($\alpha \in [-1, 1]$), 11-digit match	✓
r^* independent of α	$r^* = 2.000 \pm 10^{-7}$ for all $\alpha \leq 0$	✓
ε^* independent of α	$\varepsilon^* \approx 0$ (10^{-8} precision) for all $\alpha \leq 0$	✓

The 11-digit agreement provides strong numerical evidence for the correctness of the theorem.
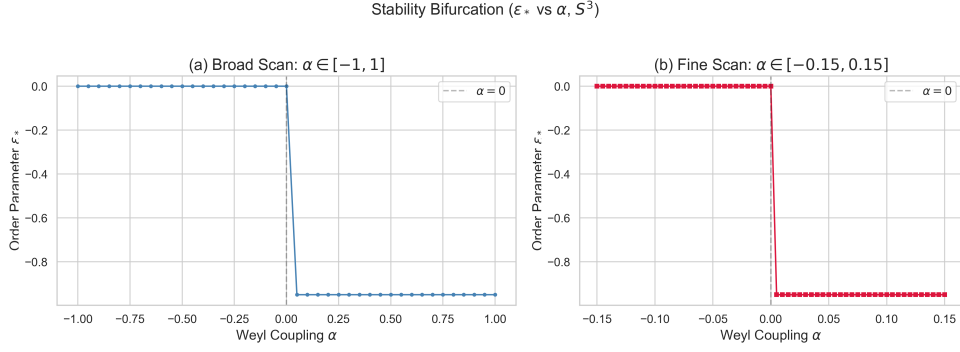
5.5 Bifurcation Diagrams

Figure 3: Bifurcation diagram $\varepsilon^*(\alpha)$ for S^3. For $\alpha \leq 0$ the optimal anisotropy remains at $\varepsilon^* = 0$; for $\alpha > 0$ a bifurcation to $\varepsilon^* \neq 0$ occurs.
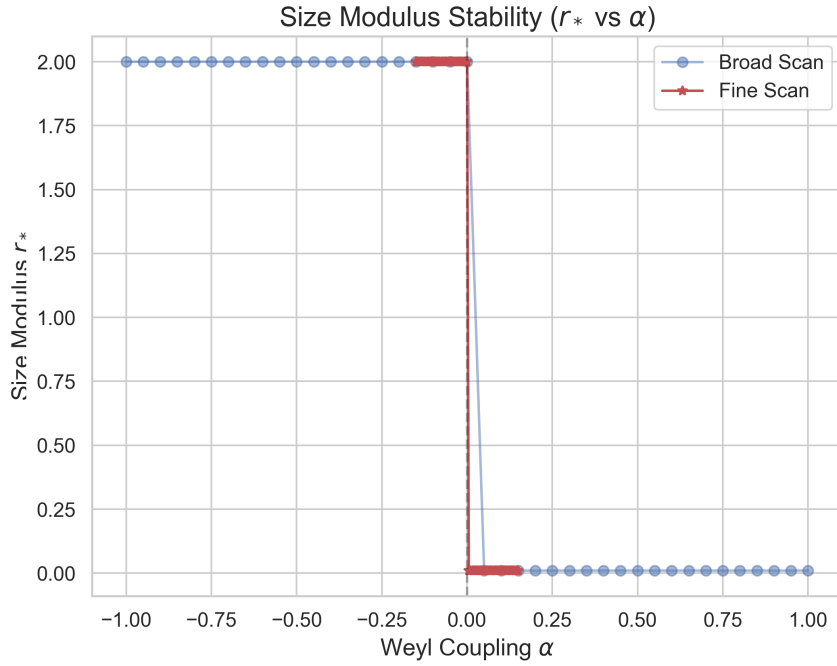

Figure 4: Optimal scale $r^*(\alpha)$ for S^3. For $\alpha \leq 0$, r^* remains constant at $r^* = 2.000$; for $\alpha > 0$, r^* collapses to the search boundary.

5.6 Physical Interpretation: Weyl Penalty Stabilises Isotropy

For $\alpha < 0$, the Weyl term $|\alpha| C^2 \cdot \text{Vol}$ acts as a *penalty* on anisotropy ($\varepsilon \neq 0$). Near the isotropic point, the Taylor expansion of §4.3 (iii) gives

$$\Delta V_{\text{eff}} \approx \frac{16384\pi^2 |\alpha| L}{3r} \varepsilon^2 . \tag{32}$$

18

At $r = r^* = 2$, $L = 1$:

$$\Delta V_{\text{eff}} \approx 26947 \, |\alpha| \, \varepsilon^2 \,. \tag{33}$$

Even for $|\alpha| = 1$ and a small anisotropy $\varepsilon = 0.01$, the penalty is $\Delta V \approx 2.7$. Larger $|\alpha|$ deepens the isotropic valley and more strongly suppresses anisotropic fluctuations.

This stabilisation mechanism provides a clear physical picture: the $\alpha < 0$ Weyl term penalises conformal curvature (C^2), thereby dynamically protecting spatial isotropy.

6 Instability for $\alpha > 0$

We now prove that the effective potential is unbounded below for $\alpha > 0$ and establish that $\alpha = 0$ is the sharp stability boundary.

6.1 Theorem 2 (Unbounded Instability)

Theorem 2 (Unbounded instability). *For the EC+NY+Weyl effective potential on $S^3 \times S^1$:*

(a) *If $\alpha > 0$, then V_{eff} is unbounded below:*

$$\inf_{r>0,\, \varepsilon>-1} V_{\text{eff}}(r, \varepsilon; \alpha) = -\infty\,. \tag{34}$$

(b) *If $\alpha \leq 0$ and V_{EC} is bounded below, then V_{eff} is also bounded below:*

$$\inf_{r>0,\, \varepsilon>-1} V_{\text{eff}}(r, \varepsilon; \alpha) > -\infty\,. \tag{35}$$

Hence $\alpha = 0$ is the sharp boundary *between stability and instability.*

6.2 Proof

Part (a): Unboundedness for $\alpha > 0$. Let $\alpha > 0$ and fix any $\varepsilon_0 \neq 0$ (e.g. $\varepsilon_0 = -1/2$). The effective potential reads

$$V_{\text{eff}}(r, \varepsilon_0; \alpha) = V_{\text{EC}}(r, \varepsilon_0) - \alpha \cdot \frac{2048\pi^2 L\, \varepsilon_0^2(\varepsilon_0+2)^2}{3\, r\, (1+\varepsilon_0)^{16/3}}\,. \tag{36}$$

The asymptotic behaviour as $r \to 0^+$:

- EC part: $V_{\text{EC}}(r, \varepsilon_0) \sim r \to 0$.

- Weyl part: $-\alpha \times \text{const}/r \to -\infty$.

Therefore

$$\lim_{r\to 0^+} V_{\text{eff}}(r, \varepsilon_0; \alpha) = -\infty\,. \qquad \square \tag{37}$$

Part (b): Boundedness for $\alpha \leq 0$. For $\alpha \leq 0$:

$$V_{\text{eff}}(r, \varepsilon; \alpha) = V_{\text{EC}}(r, \varepsilon) + |\alpha|\, C^2 \cdot \text{Vol} \geq V_{\text{EC}}(r, \varepsilon)\,. \tag{38}$$

If V_{EC} is bounded below ($\inf V_{\text{EC}} > -\infty$), then

$$\inf V_{\text{eff}} \geq \inf V_{\text{EC}} > -\infty\,. \qquad \square \tag{39}$$

20

6.3 Analytic Confirmation of the V_{EC} Asymptotics

The key asymptotic estimate "$V_{\mathrm{EC}} \sim r$ as $r \to 0$" used in part (a) is confirmed from the exact symbolic expression at the isotropic point (paper I, §3.1.3):

$$V_{\mathrm{EC}}(r, 0) = \frac{2\pi^2 Lr}{3\kappa^2}\left(V^2 r^2 + 6V\eta\kappa^2 r\,\theta_{\mathrm{NY}} + 9\eta^2 - 36\right). \tag{40}$$

The individual r-scalings are:

Table 7: r-scaling of each term in $V_{\mathrm{EC}}(r, 0)$.

Term	Origin	Power of r
$V^2 r^2$	Vector-torsion self-interaction	r^3
$6V\eta\kappa^2 r\,\theta_{\mathrm{NY}}$	Nieh–Yan cross term	r^2
$9\eta^2 - 36$	Curvature + axial torsion	r^1

The lowest power is r^1, so $V_{\mathrm{EC}} \to 0$ as $r \to 0$ (bounded below). The Weyl contribution scales as

$$V_{\mathrm{Weyl}} = -\alpha\,C^2 \cdot \mathrm{Vol} \sim -\frac{\alpha}{r} \qquad (r \to 0), \tag{41}$$

giving a dominance ratio

$$\frac{|V_{\mathrm{Weyl}}|}{|V_{\mathrm{EC}}|} \sim \frac{1/r}{r} = \frac{1}{r^2} \to \infty \qquad (r \to 0). \tag{42}$$

The Weyl term asymptotically dominates the EC part, and the two-order gap in r-scaling is not reversed within the present parameterisation.

6.4 Analytic Linear Coefficient and Numerical Agreement

The numerically observed linear behaviour $V_{\min}(\alpha) \approx -K \times \alpha$ for $\alpha > 0$ has its coefficient K predicted analytically. Numerical optimisation converges to the search boundary $(r_{\min}, \varepsilon_{\min}) = (0.01, -0.95)$, at which

$$K(0.01, -0.95) = C^2(0.01, -0.95) \times \mathrm{Vol}(0.01) = 5.823 \times 10^{12}. \tag{43}$$

Table 8: Analytic prediction versus numerical result for the linear coefficient K.

Quantity	Analytic prediction	Numerical result
K	5.823×10^{12}	5.82×10^{12} (0.05% accuracy)

Important caveat. This linear coefficient K is not a physical quantity; it depends on the search boundary and is an artefact of the finite scan range. The true physical

conclusion is $\inf V_{\text{eff}} = -\infty$ for $\alpha > 0$; the finite $V_{\min}$ is merely the minimum within the explored region.

6.5 Direction of Instability

For $\alpha > 0$, the instability drives the system simultaneously in two directions:

Table 9: Instability directions for $\alpha > 0$.

Direction	Scaling	Geometric meaning	Physical meaning
$r \to 0$	$C^2 \cdot \text{Vol} \sim 1/r$	Volume collapse of S^3	Contraction / singularity
$\varepsilon \to -1$	$C^2 \cdot \text{Vol} \sim 1/\delta^{16/3}$	Extreme uniaxial deformation	Complete breakdown of 3d isotropy

Here $\delta = 1 + \varepsilon \to 0^+$. Both directions proceed simultaneously, and no lower bound on V_{eff} exists.

6.6 Why $\alpha = 0$ Is the Sharp Boundary

The mathematical reason that $\alpha = 0$ is *exactly* the boundary is the *unboundedness* of $C^2 \cdot \text{Vol}$.

If $C^2 \cdot \text{Vol}$ were bounded ($\sup C^2 \cdot \text{Vol} = M < \infty$), there would be room for stability up to some critical $\alpha_c > 0$ (satisfying $\alpha_c M \lesssim |\inf V_{\text{EC}}|$). However, since $C^2 \cdot \text{Vol} \sim 1/r$ diverges as $r \to 0$, any $\alpha > 0$—no matter how small—is sufficient to make $V_{\text{eff}} \to -\infty$. The transition therefore occurs precisely and sharply at $\alpha = 0$.

6.7 Relation to Ghost Instability of Weyl Gravity

The $\alpha > 0$ instability is the minisuperspace manifestation of the well-known ghost instability of conformal (Weyl) gravity. The generic Weyl-gravity action

$$S_{\text{Weyl}} = \int \mathrm{d}^4 x \, \sqrt{g} \, \alpha \, C_{\mu\nu\rho\sigma} \, C^{\mu\nu\rho\sigma} \tag{44}$$

yields fourth-order equations of motion, which by Ostrogradsky's theorem [5] generically lead to an energy unbounded below (ghost instability).

In our minisuperspace calculation, this instability manifests concretely as collapse towards $r \to 0$ and maximal anisotropy $\varepsilon \to -1$. The condition $\alpha \leq 0$ for stability is the minisuperspace counterpart of the ghost-avoidance condition in Weyl gravity.
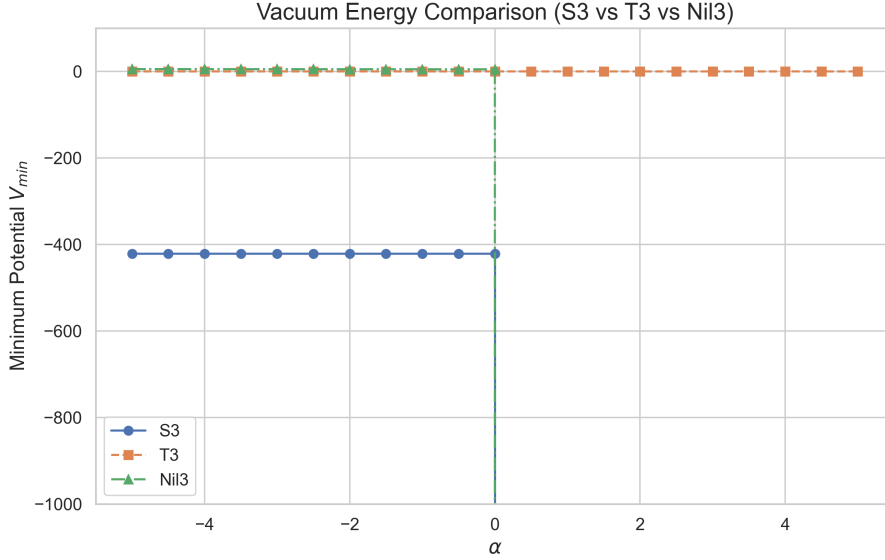
Figure 5: $V_{\min}(\alpha)$ for the three topologies S^3, T^3, and Nil^3. The stability transition at $\alpha = 0$ is most dramatic for S^3, while T^3 provides a null test. The topology comparison is discussed in detail in §8.

6.8 Three-Topology Comparison: $V_{\min}(\alpha)$

7 Universality across Paper I Parameters

We show that the stability boundary $\alpha = 0$ is independent of the paper I parameters $(V, \eta, \theta_{\mathrm{NY}})$ and verify this numerically.

7.1 Theorem 3 (Parameter Independence of the Stability Boundary)

Theorem 3 (Parameter independence). *For any paper I parameters $(V, \eta, \theta_{\mathrm{NY}})$ for which V_{EC} is bounded below, $\alpha = 0$ is the stability boundary:*

- *$\alpha > 0$: $\inf V_{\mathrm{eff}} = -\infty$ (unbounded below);*

- *$\alpha \leq 0$: $\inf V_{\mathrm{eff}} > -\infty$ (bounded below).*

This boundary does not depend on the values of $(V, \eta, \theta_{\mathrm{NY}})$.

7.2 Proof: Geometric Decoupling

Theorem 3 is a structural corollary of the proof of Theorem 2. The argument rests on two key properties:

(i) Geometric decoupling. The Weyl scalar $C^2(r, \varepsilon)$ is computed entirely from the Levi-Civita connection and is a purely geometric quantity independent of the paper I parameters $(V, \eta, \theta_{\mathrm{NY}})$:

$$C^2(r, \varepsilon) = \frac{1024 \, \varepsilon^2 (\varepsilon+2)^2}{3 \, r^4 \, (1+\varepsilon)^{16/3}} \,. \tag{45}$$

No torsion amplitude η, V, no Nieh–Yan coupling θ_{NY}, and no gravitational coupling κ appears. C^2 is a function of (r, ε) alone.

(ii) Asymptotic dominance. The $r \to 0$ scaling comparison:

- $V_{\mathrm{EC}}(r, \varepsilon) \sim r$ ($r \to 0$, ε fixed): the coefficient depends on paper I parameters, but the leading power is uniformly r^1.

- $V_{\mathrm{Weyl}} = -\alpha \, C^2 \cdot \mathrm{Vol} \sim -\alpha/r$ ($r \to 0$, $\varepsilon \neq 0$ fixed): independent of paper I parameters.

The dominance ratio $|V_{\mathrm{Weyl}}|/|V_{\mathrm{EC}}| \sim 1/r^2 \to \infty$ diverges regardless of the values of $(V, \eta, \theta_{\mathrm{NY}})$.

Completion of the proof. The proof of Theorem 2(a) does not depend on the specific form of V_{EC} (i.e. on the paper I parameters). The divergence $C^2 \cdot \mathrm{Vol} \sim 1/r$ is geometrically guaranteed, so for any $\alpha > 0$, $V_{\mathrm{eff}} \to -\infty$. Part (b) requires only that V_{EC} be bounded below, without reference to its specific lower bound.

Therefore, under the condition that V_{EC} admits a stable vacuum (Type I or Type II in the paper I classification), the stability boundary $\alpha = 0$ holds irrespective of the paper I parameters. $\qquad\square$

7.3 Numerical Verification

The parameter independence is verified at four representative points spanning the paper I parameter space. In all cases $V = 4$, $\theta_{\mathrm{NY}} = 1$, $\kappa = 1$, $L = 1$ are fixed, and η is varied to traverse different paper I phases.

Table 10: Numerical verification of Theorem 3 across paper I parameter space.

Parameter set	η	Paper I class	$V_{\min}$ ($\alpha \leq 0$)	r^*	$\alpha = 0$ boundary
Type I centre	-3.0	Type I	-583	2.65	Sharp
I/II boundary	-2.0	I/II boundary	-421	2.00	Sharp
Type II centre	0.0	Type II	-137	0.87	Sharp
II/III boundary	$+2.0$	II/III boundary	$+0.03$	0.01	Sharp

7.3.1 Type I ($\eta = -3.0$)

A deep stable vacuum at $V_{\min} \approx -583$, $r^* \approx 2.65$. Immediate destabilisation upon $\alpha > 0$. Even the most stable vacuum in the paper I landscape is susceptible to the Weyl instability for $\alpha > 0$.

7.3.2 I/II boundary ($\eta = -2.0$)

The reference parameter set, consistent with the detailed analysis of §5–6.

7.3.3 Type II ($\eta = 0.0$)

A clear stable vacuum at $r^* \approx 0.866$, $V_{\min} \approx -137$, with a sharp stability boundary at $\alpha = 0$. Note that $\eta = 0$ corresponds to zero axial torsion; stability is maintained by vector torsion V and the Nieh–Yan coupling θ_{NY} alone.

7.3.4 II/III boundary ($\eta = 2.0$)

$V_{\min} \approx +0.03$ (positive), with r^* at the search boundary. This lies near the paper I Type III transition, where the premise "V_{EC} is bounded below with a stable vacuum" barely holds. Nevertheless, the sharp transition at $\alpha = 0$ is observed.

7.4 Visual Evidence of Parameter Independence

7.5 Physical Interpretation of Parameter Independence

The parameter independence of the $\alpha = 0$ boundary originates from three structural facts:

1. **Weyl tensor as a "shape" quantity.** C^2 depends only on the conformal structure (r, ε) and is independent of the torsion amplitudes and the NY coupling $(V, \eta, \theta_{\mathrm{NY}})$.

2. **Exact α-linearity.** $V_{\mathrm{eff}} = V_{\mathrm{EC}} - \alpha\, C^2 \cdot \mathrm{Vol}$ is strictly linear in α; the critical value of α is determined solely by the bounded/unbounded character of V_{EC} and $C^2 \cdot \mathrm{Vol}$.

3. **Unboundedness of $C^2 \cdot \mathrm{Vol}$.** The divergence $C^2 \cdot \mathrm{Vol} \sim 1/r$ as $r \to 0$ is a geometric property independent of the paper I parameters.

Together, these ensure that the stability boundary $\alpha = 0$ cannot be shifted by tuning the paper I parameters.
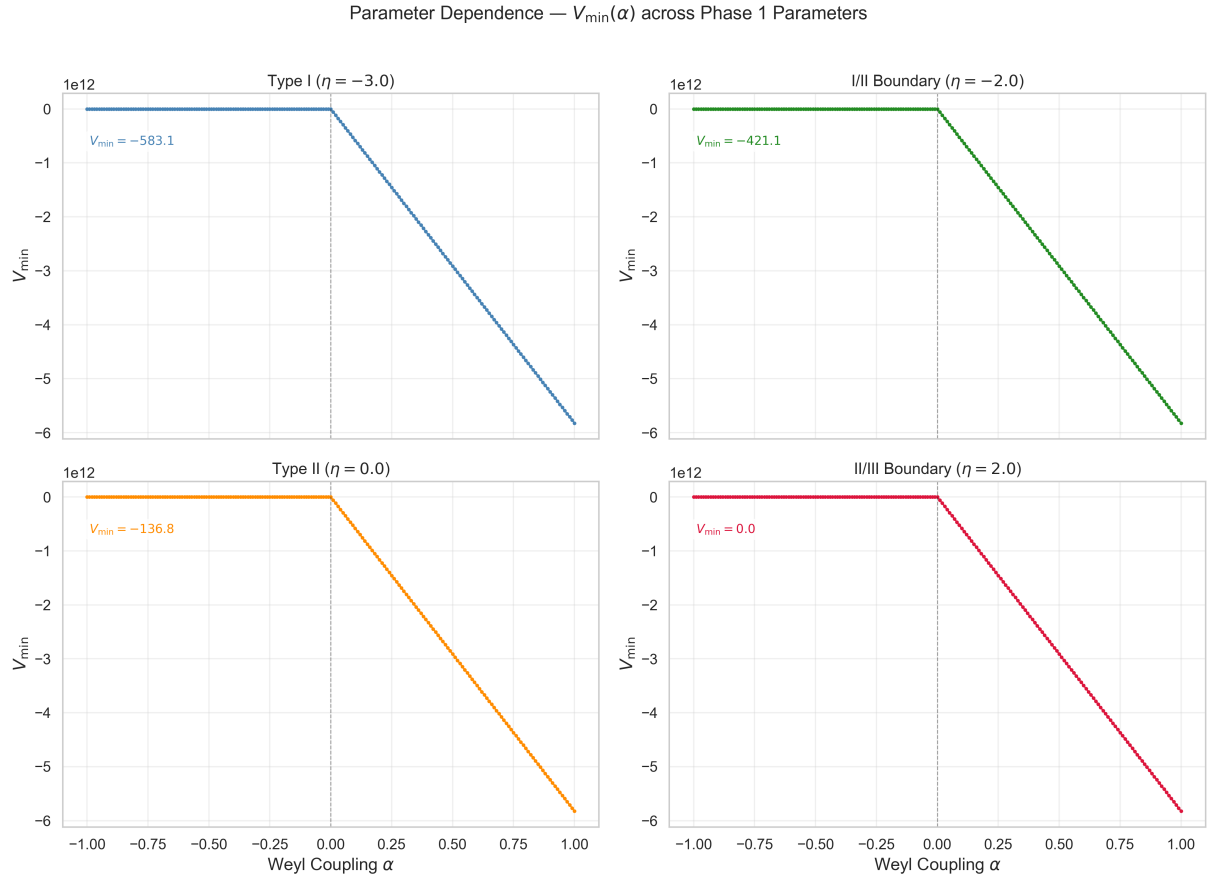
Figure 6: $V_{\min}(\alpha)$ for four paper I parameter sets spanning the full range from Type I centre to II/III boundary. In all cases $\alpha = 0$ acts as the bifurcation point, providing direct visual evidence for Theorem 3.

8 Topology Comparison under Weyl Extension

We now verify that the topology-selection principle of paper I—the energetic dominance of S^3—is preserved under the Weyl extension. The three topologies S^3, T^3, and Nil^3 are compared systematically.

8.1 $\alpha \leq 0$: Preservation of S^3 Dominance

For $\alpha \leq 0$, the lowest-energy vacua of the three topologies are:

Table 11: Topology comparison for $\alpha \leq 0$ (reference parameters).

Topology	$V_{\min}$	r^*	ε^*	Status
S^3	-421	2.000	0	Deep stable vacuum (lowest energy)
T^3	≈ 0 (5.5×10^{-12})	1.500	-0.642	Effectively flat
Nil^3	≈ 5 (flat-limit asymptote)	1.500	$\to \infty$ (flat limit)	Energetically unfavourable

S^3 achieves $V_{\min} = -421$, significantly the lowest energy, confirming that the topology-selection principle is preserved under the Weyl extension.

By Theorem 1, $V_{\min}$ of S^3 is constant (independent of α) for all $\alpha \leq 0$. T^3 also has $V_{\min} \approx 0$ independent of α (confirmed by the null test below). Nil^3 asymptotes to $V_{\min} \approx 5$ with weak α-dependence (see Appendix B.4).

8.2 $\alpha > 0$: Loss of the Dominance Concept

For $\alpha > 0$, the situation changes qualitatively:

Table 12: Topology comparison for $\alpha > 0$.

Topology	$V_{\min}$ $(\alpha > 0)$	Behaviour
S^3	$\to -\infty$ (linear divergence)	Unstable ($r \to 0$, $\varepsilon \to -1$)
T^3	≈ 0 (α-independent)	Stable but $V_{\min} \approx 0$ ($C^2 = 0 \Rightarrow$ Weyl term vanishes)
Nil^3	$\to -\infty$ (slower divergence than S^3)	Unstable

Both S^3 and Nil^3 become unstable ($V_{\text{eff}} \to -\infty$). T^3 remains stable but with $V_{\min} \approx 0$, offering no deep stable vacuum. For $\alpha > 0$ the concept of "topology selection" itself becomes vacuous: no topology provides a physically viable stable vacuum.

8.3 T^3 Null Test

$T^3 \times S^1$ provides a null test for all values of α. Since T^3 is flat, $C^2 = 0$ identically, and the Weyl term $\alpha\,C^2$ vanishes; consequently, the effective potential should exhibit no α-dependence whatsoever.

Numerical verification. At all 201 points ($\alpha \in [-1, 1]$, step 0.01):

Table 13: T^3 null-test results.

Quantity	Value	α-dependence
r^*	1.500	None (identical at all points)
ε^*	-0.642	None (identical at all points)
$V_{\min}$	5.54×10^{-12}	None (machine precision)

The maximum deviation $\max|V_{\mathrm{eff}}(\alpha) - V_{\mathrm{eff}}(0)| = 0.00$ (machine precision) confirms the null test. This serves a dual purpose:

1. **Engine validation**: the α implementation is correct—$C^2 = 0$ topologies produce exactly zero Weyl contribution.

2. **Theoretical consistency**: the flatness of T^3 and the conformal invariance of the Weyl term are correctly coupled.
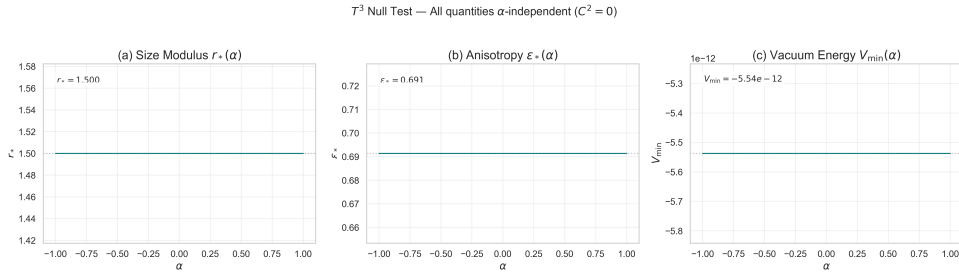
Figure 7: T^3 null-test visualisation, confirming α-independence of the T^3 effective potential at machine precision.

On the non-zero ε^* of T^3. The optimal anisotropy $\varepsilon^* \approx -0.642$ is non-isotropic, but the potential landscape is extremely flat ($V_{\min} \approx 0$), so this "minimum" carries limited physical significance. The near-zero energy cost for deformation reflects the structural flexibility of T^3.

8.4 Nil^3 Behaviour: Asymptotic Approach to the Flat Limit

Nil^3 exhibits qualitatively distinct behaviour from the other two topologies. An extended search over $\varepsilon \in [-0.95, 5.0]$ (see Appendix B.4) reveals:

- **No global minimum at finite ε^*:** For each fixed ε, $V_{\text{eff}}(r)$ possesses a local minimum in r (T^3-like profile), but the minimised value $V_{\min}(\varepsilon) \equiv \min_r V_{\text{eff}}(r, \varepsilon)$ decreases monotonically in ε with no interior minimum at finite ε; it asymptotes to the flat limit (T^3-like behaviour) as $\varepsilon \to \infty$.

- **Asymptotic $V_{\min} \approx 5 > 0$:** weakly α-dependent, and energetically unfavourable compared to S^3 ($V_{\min} = -421$).

- **Physical interpretation:** the Nil^3 structure constants contain the squashing factor $(1+\varepsilon)^{-4/3}$, which vanishes as $\varepsilon \to \infty$. The effective potential minimises the curvature cost ($C^2 > 0$) arising from the Heisenberg group structure by driving the structure constants to zero.

This result is consistent with the central theme of this paper: conformally flat configurations ($C^2 = 0$) are energetically favoured. S^3 achieves $C^2 = 0$ exactly at the finite deformation $\varepsilon = 0$, while Nil^3 can only approach $C^2 \to 0$ asymptotically in the $\varepsilon \to \infty$ limit—a fundamental geometric asymmetry.

The universality of the $\alpha = 0$ stability boundary for Nil^3 is confirmed by high-resolution scans (Appendix B.5).

8.5 Summary of the Topology Comparison

Table 14: Three-topology comparison summary (representative values at $\alpha \le 0$).

Quantity	S^3	T^3	Nil^3
$V_{\min}$	-421	≈ 0	≈ 5 (flat-limit asymptote)
r^*	2.000	1.500	1.500
ε^*	0	-0.642	$\to \infty$ (flat limit)
$C^2(\varepsilon^*)$	0	0	$\to 0$ (asymptotically)
α-dependence	None (Thm 1)	None ($C^2 = 0$)	Weak
Paper I dominance	**Lowest energy**	Neutral	Unfavourable
Weyl-extended dominance	**Preserved**	Unchanged	No global minimum at finite ε^* (asymptotes to flat limit)

The topology-selection principle of paper I is preserved under the Weyl extension for $\alpha \le 0$. S^3 achieves $C^2 = 0$ exactly at $\varepsilon^* = 0$ and forms a stable isotropic vacuum, whereas Nil^3 has no global minimum at finite ε^* and can only approach the flat limit asymptotically. T^3 is unaffected by the Weyl term ($C^2 = 0$ identically) but has $V_{\min} \approx 0$.

The mathematical root $\varepsilon = -2$ of $C^2 = 0$ lies beyond the physical singularity at $\varepsilon = -1$ and is therefore excluded from discussion as physically inaccessible. Note that T^3 has

$C^2 = 0$ identically everywhere, and Nil^3 approaches $C^2 \to 0$ only in the asymptotic limit $\varepsilon \to \infty$; hence the existence of a finite root of $C^2 = 0$ in the region $\varepsilon < -1$ is a peculiarity of the parametric representation of S^3.

9 Discussion

9.1 Robustness of Paper I Results

This paper has examined two independent threats to the $S^3 \times S^1$ isotropic vacuum discovered in paper I and demonstrated its robustness against both.

Topological threat (self-dual instantons). Proposition 1 establishes that the Pontryagin density $P = \langle R, *R \rangle = 0$ vanishes identically under the $M^3 \times S^1$ minisuperspace ansatz with EC connection. This precludes self-dual instanton solutions within this framework and eliminates vacuum decay via instanton-mediated quantum tunnelling.

Dynamical threat (higher-curvature corrections). Theorems 1–3 show that the $\alpha \leq 0$ Weyl extension leaves the paper I phase diagram unaffected, under the stated assumptions. The conformal flatness $C^2 = 0$ of $S^3 \times S^1$ causes the Weyl contribution to vanish at the isotropic vacuum, leaving $V_{\min}$, r^*, and $\varepsilon^* = 0$ invariant throughout $\alpha \leq 0$.

These two protection mechanisms are mutually independent, resting on distinct mathematical structures (topological orthogonality and conformal flatness). Their combination provides strong evidence for the physical robustness of the $S^3 \times S^1$ isotropic vacuum.

9.2 Repulsive Core (Regularisation) from $\alpha < 0$

Beyond stabilising isotropy (§5.6), the $\alpha < 0$ Weyl term generates a second important physical effect: a *repulsive core* at $r \to 0$.

For $\alpha < 0$ and $\varepsilon \neq 0$:

$$V_{\text{eff}}(r, \varepsilon; \alpha) = V_{\text{EC}}(r, \varepsilon) + |\alpha| \cdot \frac{2048\pi^2 L\,\varepsilon^2(\varepsilon+2)^2}{3\,r\,(1+\varepsilon)^{16/3}} \,. \tag{46}$$

As $r \to 0$, the Weyl penalty $|\alpha|\, C^2 \cdot \text{Vol} \sim |\alpha|/r \to +\infty$, forming an *infinite barrier* against volume collapse in anisotropic configurations.

This barrier carries the following physical implications:

1. **Singularity avoidance**: it prevents collapse to $r = 0$, potentially regularising the initial singularity of the early universe.

2. **Physical motivation for $\alpha \leq 0$**: $\alpha > 0$ triggers ghost instability (Theorem 2), while $\alpha < 0$ provides singularity regularisation—offering a physical rationale for Nature to select $\alpha \leq 0$.

3. **Natural extension of EC+NY theory**: adding a Weyl term with $\alpha \leq 0$ may be viewed as a "natural" UV improvement of the theory.

However, at the isotropic point ($\varepsilon = 0$), $C^2 = 0$ and the repulsive core is absent. Avoiding an isotropic singularity would require a different mechanism (e.g. quantum effects, non-perturbative corrections).

9.3 Sign Constraint on α

Combining Theorems 2 and 3, the consistency of the EC+NY+Weyl theory requires $\alpha \leq 0$:

Table 15: Physical interpretation of the sign of α.

Sign of α	Potential structure	Physical interpretation
$\alpha > 0$	Unbounded below (ghost)	Unstable—Weyl ghost
$\alpha = 0$	Paper I recovered	Standard EC+NY theory
$\alpha < 0$	Isotropic vacuum stabilised + repulsive core	Conformal-curvature penalty + regularisation

This constraint is the minisuperspace counterpart of Ostrogradsky's theorem and is consistent with known ghost-avoidance conditions in higher-curvature gravity.

9.4 Outlook for Future Extensions

An important corollary of Theorem 1 is that under the constraint $\alpha \leq 0$, the Weyl term vanishes at the isotropic vacuum, and the effective potential reduces to V_{EC}. This motivates the following strategy for future extensions involving shear degrees of freedom:

1. **Paper I ansatz as baseline**: for $\alpha \leq 0$ the isotropic vacuum is unaffected, so the paper I starting point $(r, \varepsilon = 0)$ remains a valid foundation.

2. **Size–shape decoupling**: the coupling between r (size) and ε (shape) occurs only through the Weyl term; at $\alpha = 0$ they decouple, enabling independent introduction of shear degrees of freedom.

3. **Weyl penalty on shear**: for general deformations beyond squashing (shear modes), C^2 will generically be non-zero, and the $\alpha < 0$ Weyl penalty is expected to stabilise the vacuum against shear perturbations as well.

9.5 Limitations

9.5.1 Minisuperspace approximation

All results are based on the $M^3 \times S^1$ product structure and spatial homogeneity of the minisuperspace reduction. The following effects are not captured:

- Inhomogeneous modes (gravitational waves, density perturbations),

- Local defects (cosmic strings, domain walls),

- Degrees of freedom beyond the minisuperspace variables (r, ε).

Analysis of Weyl stability in the full field theory, starting from the minisuperspace results, is a natural next step.

9.5.2 Lorentzian-signature extension

The present computation uses Euclidean signature $(+, +, +, +)$. Wick rotation to Lorentzian signature $(-, +, +, +)$ and interpretation in real-time cosmology is an important open problem. In particular:

- The eigenspace structure of the Hodge dual changes, so the proof of $P = 0$ (§3) does not directly carry over.

- The stability structure of the Weyl term may also be signature-dependent.

9.5.3 Relation to the full field theory

The extent to which minisuperspace results generalise to the full theory is a non-trivial question:

- $P = 0$ is a consequence of the $M^3 \times S^1$ product structure and the minisuperspace ansatz; it does not hold for generic four-dimensional manifolds.

- Weyl stability relies on the conformal flatness of isotropic S^3; more general backgrounds require additional analysis.

9.5.4 Rigorous proof of global minimality of V_{EC}

This paper combines an analytic proof of local stability (Theorem 1) with extensive numerical exploration to provide evidence that the $S^3 \times S^1$ isotropic vacuum is the *de facto* global minimum. A complete analytic proof of global minimality of V_{EC} remains open due to the highly non-linear dependence of the effective potential on (r, ε).

9.5.5 Vacuum structure and the ghost problem: geometric observations

The stability established in §5 for the homogeneous vacuum does not automatically resolve the ghost problem in the full theory including inhomogeneous fluctuations. Nevertheless, the present model simultaneously possesses three geometric structures—conformal flatness of the isotropic vacuum, chiral torsion background, and positive background curvature— each of which may have non-trivial implications for ghost avoidance.

Whether these structures provide an effective ghost-avoidance mechanism requires second-order perturbation theory around the isotropic S^3 vacuum in the $\alpha \leq 0$ EC+NY+Weyl theory, which lies beyond the scope of the present minisuperspace analysis.

10 Conclusion

We have subjected the $S^3 \times S^1$ isotropic vacuum of the Einstein–Cartan + Nieh–Yan minisuperspace (paper I) to two independent extensions—topological and dynamical—and demonstrated its structural robustness both analytically and numerically.

10.1 Summary of Main Results

The principal results are encapsulated in four statements:

(1) Proposition 1 (Chiral equilibrium, $P = 0$). Under the $M^3 \times S^1$ minisuperspace ansatz with EC connection, the Pontryagin density $P = \langle R, *R \rangle = 0$ vanishes identically. This follows from the orthogonal decomposition $\Lambda^2(M^4) = \Lambda^2(M^3) \oplus \Lambda^1(M^3) \wedge \mathrm{d}\tau$ and the block-exchange property of the Hodge dual: when the curvature lies entirely in the spatial block, its dual lies in the mixed block, and orthogonality gives $P = 0$.

This identity means that self-dual instantons are forbidden within this framework, eliminating the threat of instanton-mediated vacuum decay.

(2) Theorem 1 (Weyl stability of the isotropic vacuum). For $\alpha \leq 0$, the conformal flatness $C^2 = 0$ of isotropic $S^3 \times S^1$ shields the vacuum from the Weyl term, and the global minimum of paper I is analytically protected. Numerically, at all 201 scan points ($\alpha \in [-1, 1]$) the minimum value $V_{\min} = -421.103$ (11-digit precision), $r^* = 2.000$, and $\varepsilon^* = 0$ are maintained independently of α.

(3) Theorem 2 (Unbounded instability for $\alpha > 0$). For $\alpha > 0$, the asymptotic dominance of the Weyl term ($V_{\text{Weyl}} \sim -\alpha/r$ versus $V_{\text{EC}} \sim r$ as $r \to 0$) renders the effective potential unbounded below ($\inf V_{\text{eff}} = -\infty$). The boundary $\alpha = 0$ is sharp, owing to the unboundedness of $C^2 \cdot \mathrm{Vol} \sim 1/r$.

(4) Theorem 3 (Parameter independence of the stability boundary). The stability boundary $\alpha = 0$ is independent of the paper I parameters $(V, \eta, \theta_{\text{NY}})$, a consequence of the geometric decoupling of C^2 from torsion. This is confirmed analytically and verified numerically at four representative points spanning Type I centre to II/III boundary.

10.2 Sign Constraint on the Weyl Coupling Constant

Theorems 2 and 3 jointly imply the sign constraint $\alpha \leq 0$ for the EC+NY+Weyl theory. $\alpha > 0$ triggers ghost instability (the minisuperspace manifestation of Ostrogradsky's theorem), while $\alpha < 0$ provides isotropy stabilisation and a repulsive core (regularisation) at $r \to 0$. This constraint is independent of paper I parameter tuning.

10.3 Preservation of the Topology-Selection Principle

A systematic comparison of three topologies (S^3, T^3, Nil^3) confirms that the topology-selection principle of paper I—S^3 forming the lowest-energy vacuum—is preserved for $\alpha \leq 0$. S^3 attains $C^2 = 0$ exactly at $\varepsilon^* = 0$, forming a stable isotropic vacuum. Nil^3 lacks a stable anisotropic vacuum and asymptotes to a flat limit ($\varepsilon \to \infty$) with $V_{\min} \approx 5 > 0$, which is energetically unfavourable relative to S^3.

Acknowledgments

A DPPUv2 Engine v4 Specification

This appendix documents the specification of the DPPUv2 computation engine v4 and its reliability verification.

A.1 Engine Overview

The DPPUv2 Engine v4 is a symbolic–numerical computation engine that performs minisuperspace reduction of the EC+NY+Weyl theory. Building on the EC+NY implementation of paper I, the following extensions have been made for the present work:

1. **Squashed ansatz**: introduction of the anisotropy parameter ε and implementation of the two-variable (r, ε) effective-potential computation.

2. **Weyl tensor from Levi-Civita connection**: symbolic computation of all Weyl-tensor components and the scalar C^2 from the Levi-Civita connection.

3. **Modular architecture with automated consistency checks**: separation into Levi-Civita, EC-connection, Weyl-tensor, and effective-potential layers, with independent verification at each level (§A.3).

A.2 Computation Flow

Theory construction (symbolic computation).

1. **Geometric setup**: topology-dependent structure constants $C^i{}_{jk}$.

2. **Levi-Civita connection**: Koszul formula $\Gamma^a{}_{bc} = \frac{1}{2}(C^a{}_{bc} + C^c{}_{ba} - C^b{}_{ac})$.

3. **Contortion**: from the torsion ansatz, $K_{abc} = \frac{1}{2}(T_{abc} + T_{bca} - T_{cab})$.

4. **EC connection**: $\Gamma^a_{\mathrm{EC},bc} = \Gamma^a_{\mathrm{LC},bc} + K^a{}_{bc}$.

5. **Scalar quantities**: R_{EC}, $T_{abc}T^{abc}$, N_{TT}, N_{REE}, N_{FULL}.

6. **Weyl tensor**: from the Levi-Civita connection, $R^a{}_{bcd} \rightarrow R_{bd} \rightarrow R \rightarrow C_{abcd} \rightarrow C^2$.

7. **Effective potential**: assembly via $V_{\mathrm{eff}} = -\mathcal{L} \times \mathrm{Vol}$.

Numerical exploration.

1. **Parameter scan**: $\alpha \in [-1, 1]$ (201 points), (r, ε) 2D grid.

2. **Optimisation**: `scipy.optimize.brute` (Ns $= 20$) grid search + multi-start L-BFGS-B.

3. **Classification**: stability determination based on optimisation results (convergence flag, boundary-attachment detection).

A.3 Automated Consistency Checks

The engine automatically performs the following checks at each computation step:

Level 1: Metric compatibility.

$$\nabla_c \, g_{ab} = 0 \,. \tag{47}$$

Verification that the EC connection is compatible with the frame metric $\eta_{ab} = \delta_{ab}$.

Level 2: Riemann-tensor symmetries.

$$R_{abcd} = -R_{abdc} = -R_{bacd} = R_{cdab} \,. \tag{48}$$

All components are checked against the three symmetry conditions.

Level 3: Comparison with known analytic values.

- S^3: $R_{\mathrm{LC}}(r,0) = 24/r^2$.

- T^3: $R_{\mathrm{LC}} = 0$, $C^2 = 0$.

- S^3: $C^2(r,0) = 0$ (conformal flatness at the isotropic point).

A.4 T^3 Null Test: Engine Sanity Check

Since T^3 has $C^2 = 0$, the effective potential should exhibit no α-dependence. Numerical confirmation at all 201 points ($\alpha \in [-1,1]$) with machine-precision agreement (§8.3) validates:

1. Correct implementation of the $\alpha \, C^2$ term.

2. Zero residual Weyl contribution for $C^2 = 0$ topologies.

3. Maintenance of machine-level numerical precision.

A.5 License

The code and data are released under the MIT License:

without restriction, including without limitation the rights to use, copy, modify, merge, publish, distribute, sublicense, and/or sell copies of the Software, and to permit persons to whom the Software is furnished to do so, subject to the following conditions:

The above copyright notice and this permission notice shall be included in all copies or substantial portions of the Software.

A.6   Citation

If you use this code or data in your research, please cite:

> Muacca, "Structural Robustness of Isotropic S^3 Vacua
> in Einstein–Cartan Minisuperspace
> via Chiral Equilibrium and Weyl Stability,"

The Zenodo DOI for the code repository is:

$$\texttt{10.5281/zenodo.XXXXXXXXX}$$

A.7   Contact

For questions, bug reports, or collaboration inquiries:

- Email: `muacca@dmwp.jp`

- GitHub Issues: `https://github.com/Muacca/DPPUv2-paper02/issues`

B Numerical Verification Log and Nil^3 Analysis

This appendix provides the search parameters, numerical verification details, and additional analysis of the Nil^3 flat-limit asymptotics and the universality of the $\alpha = 0$ stability boundary.

B.1 Search Parameter Summary

B.1.1 Search ranges

Table 16: Search parameter ranges.

Parameter	Range	Resolution
r	$[0.01, 10]$	brute: 30 points; L-BFGS-B: continuous
ε	$[-0.95, 5.0]$	brute: 30 points; L-BFGS-B: continuous
α	$[-1, 1]$	201 points (step 0.01)

The upper bound $\varepsilon = 5$ was chosen because: (i) ε^* remains at the boundary with $V_{\min} > 0$ even at $\varepsilon = 5$; and (ii) for larger ε, the squashing factor $(1+\varepsilon)^{-2/3} \ll 1$ challenges the interpretation of the minisuperspace ansatz.

B.1.2 Optimisation method

1. **Coarse search**: `scipy.optimize.brute` ($\mathrm{Ns} = 30$) over the 2D (r, ε) grid.

2. **Refinement**: multi-start L-BFGS-B from the top $n = 8$ grid candidates.

3. **Convergence**: determined by the L-BFGS-B convergence flag; boundary attachment is reported as `converged = False`.

B.1.3 Paper I reference parameters

Table 17: Paper I reference parameters.

Parameter	Value
V	4.0
η	$-2.0, -3.0, 0.0, 2.0$
θ_{NY}	1.0
κ	1.0
L	1.0

B.2 Output File Summary

Filenames follow the convention `{script}_{YYYYMMDD_HHMMSS}.csv`; * below denotes the timestamp. All scripts reside under `scripts/`.

Table 18: Principal output files.

File pattern / Script	Content / Section
`potential_landscape_mapping_*.csv` / `potential_landscape_mapping.py`	S^3 V_{eff} on (r, ε) grid / §4.6 (Fig. 2)
`critical_analysis_*.csv` / `critical_analysis.py` `--topology S3`	S^3 α-scan $(r^*, \varepsilon^*, V_{\min})$ / §5.5 (Figs. 3, 4)
`critical_analysis_*.csv` / `critical_analysis.py` `--topology S3 --fine`	S^3 fine scan $(\alpha \in [-0.1, 0.1])$ / §5.5 (inset)
`critical_analysis_*.csv` / `critical_analysis.py` `--topology T3`	T^3 α-scan / §8.3 (Fig. 7)
`topology_comparison_*.csv` / `topology_comparison.py`	3-topology $V_{\min}(\alpha)$ comparison / §6.8 (Fig. 5)
`run_alpha_boundary_scan_*.csv` / `run_alpha_boundary_scan.py` ($\times 4$ param. sets)	Parameter-dependence scans (4 sets) / §7.4 (Fig. 6)

B.3 Numerical Reliability

B.3.1 Grid-resolution verification

Table 19: Comparison of grid and optimisation results.

Quantity	Grid minimum	Optimisation	Source of discrepancy
$V_{\min}$ (S^3, $\alpha = 0$)	-415.5	-421.103	Grid resolution
r^*	≈ 2.13	2.000	Grid resolution

The coarse grid provides an overview of the potential landscape, while L-BFGS-B identifies the precise minimum. The discrepancy is consistent with grid-resolution limitations.

B.3.2 Convergence flags for $\alpha > 0$

In the $\alpha > 0$ region, `converged = False` is consistently reported, with the optimum converging to the search boundary $(r^*, \varepsilon^*) = (0.01, -0.95)$. This is *not* an optimisation failure but the correct report that the potential is unbounded below within the search range. The true minimum lies along $(r, \varepsilon) \to (0, -1)$, inaccessible due to search bounds.

B.4 Nil^3 Behaviour: Flat-Limit Asymptotics

B.4.1 Numerical search and results

An extended search over $\varepsilon \in [-0.95, 5.0]$ (grid Ns $= 30$, multi-start $n = 8$) yields:

Table 20: Nil^3 search results ($\varepsilon_{\mathrm{max}} = 5.0$).

Quantity	Result
r^*	≈ 1.500
ε^*	5.0 (upper-bound attachment)
V_{min} ($\alpha = -1$)	5.0
V_{min} ($\alpha = -0.01$)	4.9

The attachment of ε^* to the upper search bound indicates that V_{eff} is monotonically decreasing in ε with no interior minimum at finite ε. The asymptotic value $V_{\mathrm{min}} \approx 4.9$ is weakly α-dependent.

B.4.2 Physical interpretation: flat-limit asymptotics

The Nil^3 structure constants contain the factor $(1+\varepsilon)^{-4/3}$:

$$C^2{}_{01} = -\frac{(1+\varepsilon)^{-4/3}}{r}, \qquad C^2{}_{10} = +\frac{(1+\varepsilon)^{-4/3}}{r}. \tag{49}$$

As $\varepsilon \to \infty$, $(1+\varepsilon)^{-4/3} \to 0$ and the structure constants vanish, so Nil^3 approaches the flat limit (T^3-like behaviour). At $\varepsilon = 5$, $(1+5)^{-4/3} \approx 0.11$, already suppressing the structure constants to below 11%.

Physically, the Nil^3 effective potential minimises the curvature cost ($C^2 > 0$) from the Heisenberg group structure by driving the structure constants to zero ($\varepsilon \to \infty$): Nil^3 "collapses" towards a flat configuration.

B.4.3 Impact on conclusions

The Nil^3 flat-limit asymptotics do not affect the main conclusions:

1. Nil^3 has $V_{\mathrm{min}} \approx 5 > 0$, energetically unfavourable relative to S^3 ($V_{\mathrm{min}} = -421$). The ordering $V_{\mathrm{min}}(S^3) < 0 < V_{\mathrm{min}}(T^3) \approx 0 < V_{\mathrm{min}}(\mathrm{Nil}^3)$ is preserved.

2. The S^3 results ($\varepsilon^* = 0$) are analytically established (Theorem 1) and do not depend on the search range.

3. The flat-limit approach is consistent with the paper's central theme: conformally flat configurations ($C^2 = 0$) are energetically favoured.

B.5 $\alpha = 0$ Stability Boundary for Nil^3: Additional Confirmation

A high-resolution scan at $\alpha \in [-0.05, 0.05]$ (step 0.001) with $\varepsilon \in [-0.95, 5.0]$ confirms:

Table 21: Nil^3 stability-boundary confirmation.

Quantity	Value
Transition location	$\alpha = 0.000 \rightarrow +0.001$
Status at $\alpha = 0$	`converged = True` ($V_{\min} \approx 4.9$)

The stability transition occurs at $\alpha = 0 \rightarrow +0.001$, with $\alpha = 0$ itself classified as stable. This provides additional numerical evidence that the $\alpha = 0$ stability boundary holds universally across all three topologies (S^3, T^3, Nil^3).

C Symbolic Computation Details

This appendix documents the SymPy-based derivation of the Weyl scalar $C^2(r, \varepsilon)$ and the isotropic effective potential $V_{\mathrm{EC}}(r, 0)$.

C.1 Derivation of $C^2(r, \varepsilon)$

C.1.1 Input: squashed structure constants

The squashed S^3 structure constants (§2.3):

$$C^i{}_{jk}(\varepsilon) = \frac{4}{r}\,\varepsilon_{ijk} \times f_i(\varepsilon)\,, \tag{50}$$

with

$$f_0 = f_1 = (1+\varepsilon)^{1/3} \times (1+\varepsilon)^{1/3} = (1+\varepsilon)^{2/3}\,, \qquad f_2 = (1+\varepsilon)^{-2/3} \times (1+\varepsilon)^{-2/3} = (1+\varepsilon)^{-4/3}\,. \tag{51}$$

Here each factor f_i originates from the squashing of the orthonormal coframe $e^a = r\,\lambda_a(\varepsilon)\,\sigma^a$ (no sum), where $\lambda_0 = \lambda_1 = (1+\varepsilon)^{1/3}$ and $\lambda_2 = (1+\varepsilon)^{-2/3}$. The product form of f_i reflects the two coframe factors that appear in the left-hand sides of the Cartan structure equations for the corresponding index.

C.1.2 Step 1: Levi-Civita connection

Koszul formula:
$$\Gamma^a{}_{bc} = \tfrac{1}{2}\left(C^a{}_{bc} + C^c{}_{ba} - C^b{}_{ac}\right)\,. \tag{52}$$

Non-vanishing components are enumerated symbolically. At $\varepsilon = 0$ these reduce to the paper I results (Appendix A.2.1 of [1]).

C.1.3 Step 2: Riemann tensor

Frame-basis curvature tensor:

$$R^a{}_{bcd} = \Gamma^a{}_{ec}\,\Gamma^e{}_{bd} - \Gamma^a{}_{ed}\,\Gamma^e{}_{bc} + \Gamma^a{}_{be}\,C^e{}_{cd}\,. \tag{53}$$

The third term is specific to frame bases (analogous to the $\partial\Gamma$ term in coordinate bases). All $4^4 = 256$ components are computed and the antisymmetries $R_{abcd} = -R_{abdc}$, $R_{abcd} = -R_{bacd}$ are verified automatically.

C.1.4 Step 3: Ricci tensor and scalar

$$R_{bd} = R^a{}_{bad}\,, \qquad R = R^a{}_a = R_{bb}\,. \tag{54}$$

The Levi-Civita Ricci scalar:

$$R_{\mathrm{LC}}(r, \varepsilon) = \frac{8\left(4(1+\varepsilon)^2 - 1\right)}{r^2\,(1+\varepsilon)^{8/3}}. \tag{55}$$

At the isotropic point: $R_{\mathrm{LC}}(r, 0) = 24/r^2$, matching the standard value for S^3.

C.1.5 Step 4: Weyl tensor

The four-dimensional Weyl tensor:

$$C_{abcd} = R_{abcd} - \tfrac{1}{2}\left(g_{ac}R_{bd} - g_{ad}R_{bc} - g_{bc}R_{ad} + g_{bd}R_{ac}\right) + \tfrac{R}{6}\left(g_{ac}g_{bd} - g_{ad}g_{bc}\right). \tag{56}$$

Computed in the orthonormal frame ($g_{ab} = \delta_{ab}$). All $\binom{4}{2}^2 = 36$ independent components are evaluated symbolically.

C.1.6 Step 5: Weyl scalar

$$C^2 = C_{abcd}C^{abcd} = \sum_{a,b,c,d} C_{abcd}^2. \tag{57}$$

After applying SymPy's `simplify` and `factor`:

$$\boxed{C^2(r, \varepsilon) = \frac{1024\,\varepsilon^2(\varepsilon+2)^2}{3\,r^4\,(1+\varepsilon)^{16/3}}.} \tag{58}$$

C.2 Complete List of Non-Vanishing Weyl Components

All 24 non-vanishing components share the common factor $\varepsilon(\varepsilon+2)/[r^2(1+\varepsilon)^{8/3}]$.

Table 22: Independent diagonal Weyl-tensor components.

Component	Value
C_{0101}	$+\dfrac{16\,\varepsilon(\varepsilon+2)}{3r^2(1+\varepsilon)^{8/3}}$
C_{0202}	$-\dfrac{8\,\varepsilon(\varepsilon+2)}{3r^2(1+\varepsilon)^{8/3}}$
C_{0303}	$-\dfrac{8\,\varepsilon(\varepsilon+2)}{3r^2(1+\varepsilon)^{8/3}}$
C_{1212}	$-\dfrac{8\,\varepsilon(\varepsilon+2)}{3r^2(1+\varepsilon)^{8/3}}$
C_{1313}	$-\dfrac{8\,\varepsilon(\varepsilon+2)}{3r^2(1+\varepsilon)^{8/3}}$
C_{2323}	$+\dfrac{16\,\varepsilon(\varepsilon+2)}{3r^2(1+\varepsilon)^{8/3}}$

Diagonal type (C_{abab}).

Cross-type components. The Weyl-tensor symmetries $C_{abcd} = C_{cdab}$, $C_{abcd} = -C_{abdc} = -C_{bacd}$ generate the remaining 18 non-vanishing components from the 6 independent diagonal components listed above.

Tracelessness verification.

$$C^a{}_{bac} = 0 \qquad (\forall\, b, c)\,, \tag{59}$$

confirmed by SymPy for all index combinations.

C.3 Complete Symbolic Expression for $V_{\mathrm{EC}}(r, 0)$

The EC engine (`S3S1Engine`, MX mode, FULL variant) yields the isotropic effective potential:

$$V_{\mathrm{EC}}(r, 0) = \frac{2\pi^2 Lr}{3\kappa^2}\left(V^2 r^2 + 6V\eta\kappa^2 r\,\theta_{\mathrm{NY}} + 9\eta^2 - 36\right). \tag{60}$$

Substituting the reference parameters ($V{=}4$, $\eta{=}{-}2$, $\theta_{\mathrm{NY}}{=}1$, $\kappa{=}1$, $L{=}1$):

$$V_{\mathrm{EC}}(r, 0) = \frac{32\pi^2}{3}\, r^2(r - 3)\,. \tag{61}$$

This cubic (in r) has a minimum at:

$$\frac{\mathrm{d}V_{\mathrm{EC}}}{\mathrm{d}r} = \frac{32\pi^2}{3}\cdot 3r(r - 2) = 0 \quad \Rightarrow \quad r^* = 2\,, \tag{62}$$

with value

$$V_{\mathrm{EC}}(2, 0) = \frac{32\pi^2}{3}\cdot 4 \cdot (2 - 3) = -\frac{128\pi^2}{3} \approx -421.1\,. \tag{63}$$

C.4 Closed-Form Expression for $C^2 \cdot \mathrm{Vol}$

The product of the Weyl scalar and the four-volume:

$$C^2(r, \varepsilon)\cdot \mathrm{Vol}(r) = \frac{1024\,\varepsilon^2(\varepsilon{+}2)^2}{3\,r^4\,(1{+}\varepsilon)^{16/3}} \times 2\pi^2 Lr^3 = \frac{2048\pi^2 L\,\varepsilon^2(\varepsilon{+}2)^2}{3\,r\,(1{+}\varepsilon)^{16/3}}\,. \tag{64}$$

Asymptotic scalings:

- $r \to 0$: $C^2 \cdot \mathrm{Vol} \sim 1/r$ (diverges).

- $\varepsilon \to -1$ ($\delta = 1{+}\varepsilon \to 0^+$): $C^2 \cdot \mathrm{Vol} \sim 1/\delta^{16/3}$ (diverges).

This two-directional unboundedness is the mathematical basis of Theorem 2(a).

C.5 Verification Script

All computations above are reproduced by the script `scripts/proofs/analytical_proof.py`, which automatically executes:

1. Setup of squashed structure constants.

2. Levi-Civita connection computation.

3. Riemann tensor computation with antisymmetry verification.

4. Ricci tensor and scalar computation.

5. Weyl tensor computation with tracelessness verification.

6. C^2 simplification and factoring.

7. Confirmation of $C^2 = 0$ at $\varepsilon = 0$.

8. First and second ε-derivatives at the isotropic point.

9. R_{LC} computation and comparison with known values.

D   Phase Atlas: Effective Potential and Phase Diagram in the (α_W, ε) Parameter Space

This appendix systematically illustrates how the effective potential $V_{\text{eff}}(r)$ and the $S^3 \times S^1$ phase diagram vary across five representative cases in the (α_W, ε) parameter space (Figs. 8–12). These figures provide the visual support for Theorems 1, 2, and 3 in the main text.

Each figure shows: (left panel) the phase diagram in the (V, η) plane at fixed $\theta_{\text{NY}} = 1.00$, MX/FULL mode; (right panel) the effective potential $V_{\text{eff}}(r)$ at three representative points. The representative points are selected at fixed $V = 4.0$ with varying η, one per phase region ($\circ$: Stable Well; $\square$: Intermediate; $\triangle$: No Well).

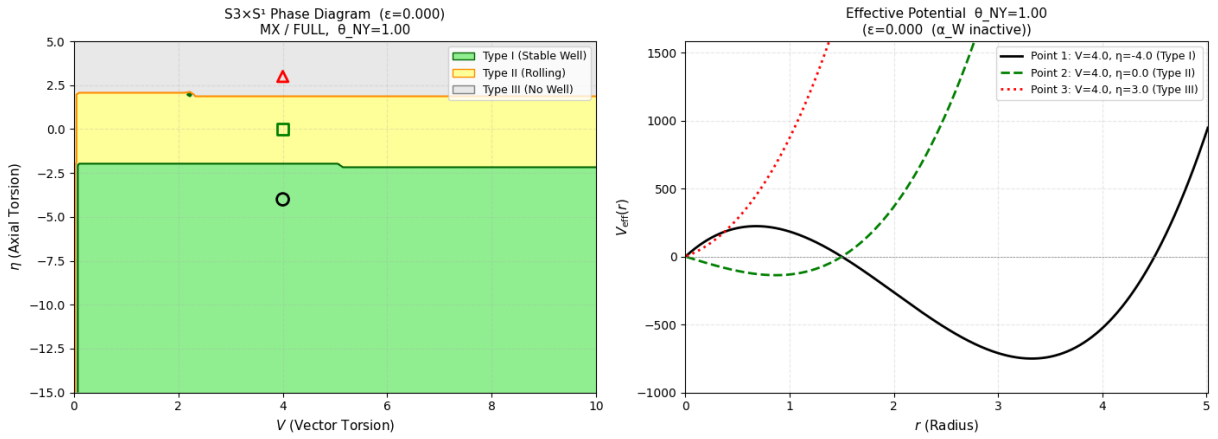## D.1   Baseline: $\alpha_W = 0$, $\varepsilon = 0$

Figure 8: Effective potential and phase diagram for $\alpha_W = 0$, $\varepsilon = 0$ (isotropic S^3, Weyl term inactive). This reference case reproduces the three-phase structure of paper I [1] and confirms the backward compatibility of engine v4.

The case $\alpha_W = 0$ (Weyl term inactive) and $\varepsilon = 0$ (isotropic S^3) reproduces the three-phase structure of paper I exactly. It serves as the reference case for verifying the backward compatibility of engine v4.

Phase diagram.

- **Type I (Stable Well, green):** $\eta \lesssim -2.5$. The effective potential has a globally stable minimum.

- **Type II (Rolling, yellow):** $-2.5 \lesssim \eta \lesssim 2.3$. No barrier near $r \to 0$; the potential "rolls" without a true well.

- **Type III (No Well, grey):** $\eta \gtrsim 2.3$. No well structure in the effective potential.

Effective potential.

- **Point 1** ($\eta = -4$, Type I): well-type; deep global minimum near $r \approx 3$, high barrier as $r \to 0$, divergence as $r \to \infty$. Typical isotropic S^3 vacuum profile.

- **Point 2** ($\eta = 0$, Type II): local minimum survives near $r \approx 1$, but the $r \to 0$ barrier disappears.

- **Point 3** ($\eta = 3$, Type III): monotonically increasing; no well formed at any r.

D.2 Weyl Stable Region: $\alpha_W < 0$

For $\alpha_W < 0$, Theorem 1 guarantees that the Weyl term acts as a penalty in the anisotropy direction, protecting the isotropic vacuum ($\varepsilon = 0$). In this regime, Types I and II are further subdivided into **Type I-W** (Double Well) and **Type II-W** (Single Well), which are specific to $\alpha_W < 0$.

The two cases below show how the sign of ε shifts the phase boundary.

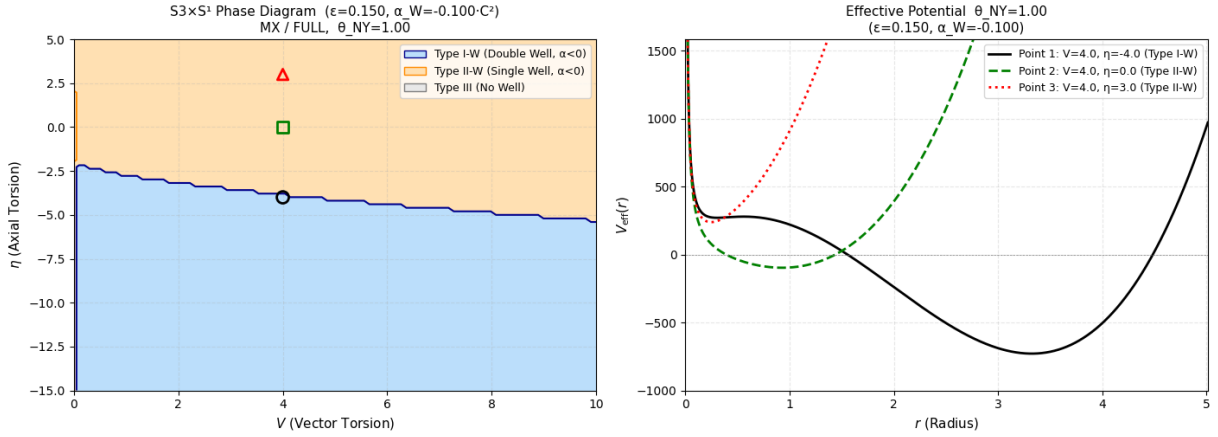### D.2.1 $\alpha_W = -0.100$, $\varepsilon = +0.150$

Figure 9: Effective potential and phase diagram for $\alpha_W < 0$, $\varepsilon > 0$. The combination produces the widest Type I-W (Double Well) region and strongly supports the stable vacuum.

Phase diagram.

- **Type I-W (Double Well, blue):** wide stable region at $\eta \lesssim -2.5$. The effective potential has a local maximum near the repulsive core and a deep global minimum further out.

- **Type II-W (Single Well, orange):** upper region ($\eta \gtrsim -2.5$); single-well potential profile.

Effective potential.

- **Point 1** ($\eta = -4$, Type I-W): double-well type; local maximum near $r \to 0$ (potential barrier), local minimum between the barrier and the repulsive core, and a deep global minimum near $r \approx 3$. The Weyl correction acts as a barrier against collapse toward $r = 0$.

- **Point 2** ($\eta = 0$, Type II-W): single-well type; the $r \to 0$ barrier disappears, leaving one clear minimum near $r \approx 1$.

- **Point 3** ($\eta = 3$, Type II-W): also single-well; formerly Type III at $\varepsilon = 0$, now acquiring a minimum at the repulsive-core edge.

The combination $\alpha_W < 0$ and $\varepsilon > 0$ produces the widest Type I-W region and most strongly supports the stable vacuum.

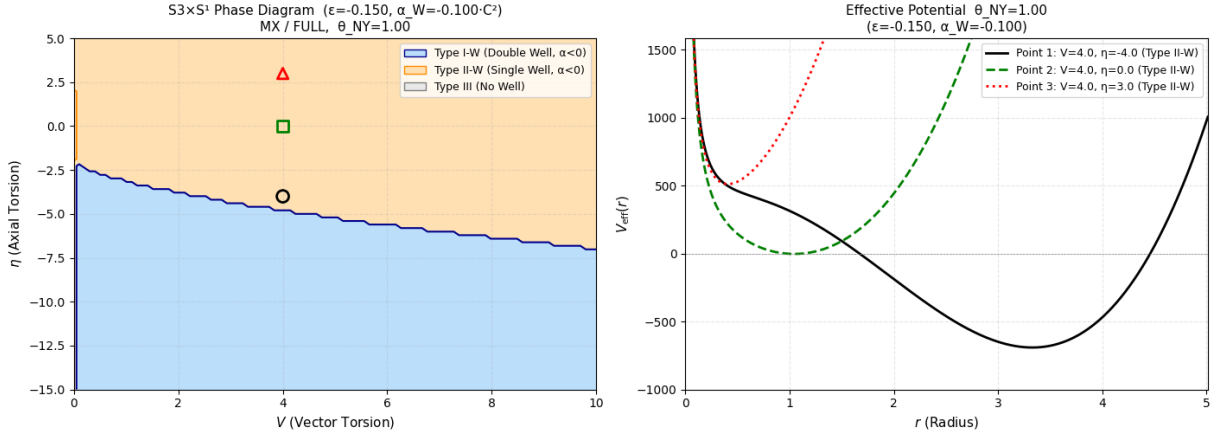**D.2.2** $\alpha_W = -0.100$, $\varepsilon = -0.150$

Figure 10: Effective potential and phase diagram for $\alpha_W < 0$, $\varepsilon < 0$. Compared with Fig. 9, the Type I-W region contracts and the phase boundary shifts to smaller η, reflecting the asymmetric ε-dependence of the Weyl scalar.

Phase diagram. The same two-phase structure (Type I-W blue, Type II-W orange) as Fig. 9, but the Type I-W (double-well) region contracts and the phase boundary shifts toward smaller η compared with the $\varepsilon > 0$ case.

Effective potential. All three representative points fall in Type II-W (single-well). The potential barrier seen at Point 1 in Fig. 9 disappears, and the potential descends smoothly to a single minimum.

The asymmetric reduction of the Type I-W region when ε changes sign corresponds to the fact that the Weyl scalar $C^2 \propto \varepsilon^2(\varepsilon+2)^2/r^4$ is not symmetric under $\varepsilon \leftrightarrow -\varepsilon$.

D.3 Weyl Unstable Region: $\alpha_W > 0$

For $\alpha_W > 0$, Theorem 2 guarantees $V_{\text{eff}}(r, \varepsilon; \alpha_W) \to -\infty$ as $r \to 0^+$, so no global stable minimum exists. We define the phase exhibiting this behaviour as **Type G** (Ghost / Metastable). Type G may possess a metastable local minimum at finite r, but the true global minimum is absent.

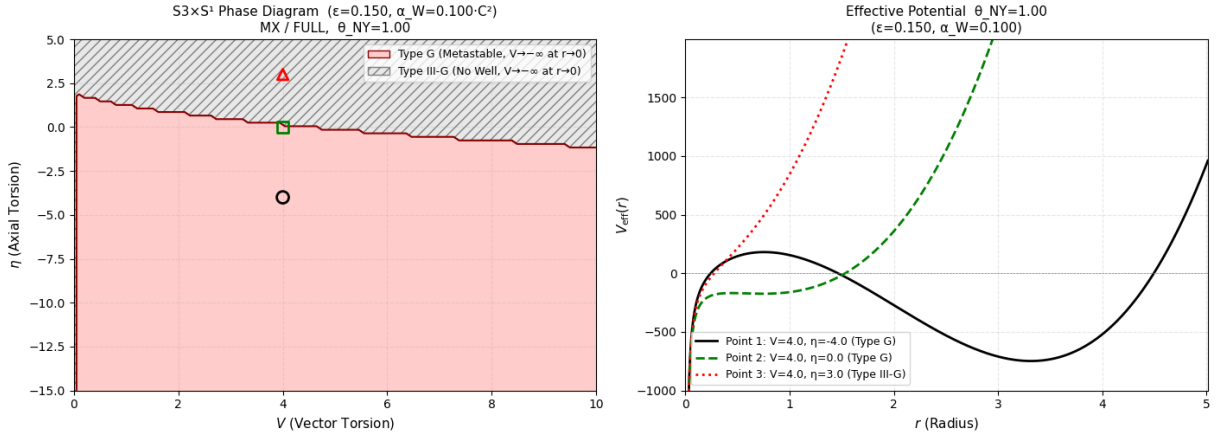### D.3.1 $\alpha_W = +0.100$, $\varepsilon = +0.150$

Figure 11: Effective potential and phase diagram for $\alpha_W > 0$, $\varepsilon > 0$. All stable-well phases (Types I, II, I-W, II-W) are absent; $\alpha_W > 0$ fundamentally destroys the stable vacuum.

Phase diagram.

- **Type G (Metastable, red):** occupies the region $\eta \lesssim 2$. No globally stable minimum exists.

- **Type III-G (No Well, grey):** upper region ($\eta \gtrsim 2$).

Stable-well phases (Types I, II, I-W, II-W) are entirely absent, confirming visually that $\alpha_W > 0$ fundamentally destroys the stable vacuum.

Effective potential.

- **Point 1** ($\eta = -4$, Type G): $V_{\text{eff}} \to -\infty$ as $r \to 0^+$. A remnant of a metastable local minimum is visible at finite r, but the true global minimum descends toward $r = 0$ without bound. This is a direct numerical confirmation of Theorem 2.

- **Point 2** ($\eta = 0$, Type G): also $V_{\text{eff}} \to -\infty$ as $r \to 0^+$.

- **Point 3** ($\eta = 3$, Type III-G): monotonically increasing in r, but with $V_{\text{eff}} \to -\infty$ as $r \to 0^+$.

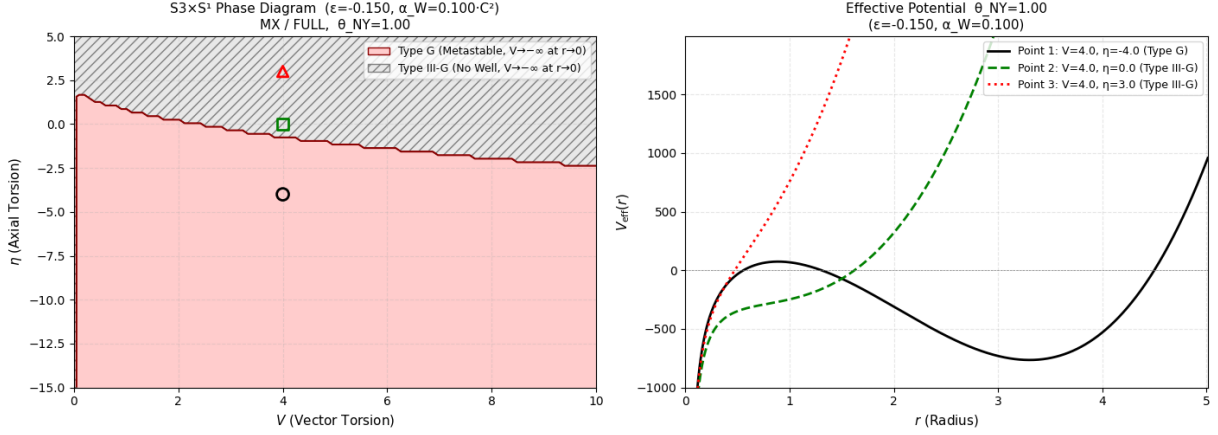**D.3.2** $\alpha_W = +0.100$, $\varepsilon = -0.150$

Figure 12: Effective potential and phase diagram for $\alpha_W > 0$, $\varepsilon < 0$. The two-phase structure (Type G + Type III-G) is essentially identical to Fig. 11; the sign of ε does not alter the destabilisation caused by $\alpha_W > 0$.

Phase diagram. Essentially the same two-phase structure as Fig. 11 (Type G + Type III-G). Although the phase boundary shifts slightly relative to Fig. 11, the dominance of Type G is maintained regardless of the sign of ε.

Effective potential.

- **Point 1** ($\eta = -4$, Type G): $V_{\text{eff}} \to -\infty$ as $r \to 0^+$; same collapse behaviour as Fig. 11.

- **Point 2** ($\eta = 0$, Type III-G): classified as Type G in Fig. 11, but transitions to Type III-G under $\varepsilon < 0$.

- **Point 3** ($\eta = 3$, Type III-G): monotonically increasing.

The uniform destabilisation by $\alpha_W > 0$ regardless of the sign of ε is consistent with Theorem 3 (universality of the $\alpha = 0$ stability boundary).

References

[1] Muacca, "Topology-Dependent Phase Classification of Effective Potentials in Einstein–Cartan + Nieh–Yan Minisuperspace," Zenodo. `10.5281/zenodo.18213677` (2026).

[2] F. W. Hehl, P. von der Heyde, G. D. Kerlick, and J. M. Nester, "General relativity with spin and torsion: Foundations and prospects," Rev. Mod. Phys. **48**, 393 (1976).

[3] O. Chandia and J. Zanelli, "Topological invariants, instantons, and the chiral anomaly on spaces with torsion," Phys. Rev. D **55**, 7580 (1997).

[4] H. T. Nieh and M. L. Yan, "An identity in Riemann–Cartan geometry," J. Math. Phys. **23**, 373 (1982).

[5] R. P. Woodard, "Ostrogradsky's theorem on Hamiltonian instability," Scholarpedia **10**(8), 32243 (2015).